RESEARCH ARTICLE | SEPTEMBER 19 2024

Optimal demodulation domain for microwave SQUID multiplexers in presence of readout system noise

M. E. García Redondo ✉ 📵 ; N. A. Müller 📵 ; J. M. Salum 📵 ; L. P. Ferreyro 📵 ; J. D. Bonilla-Neira 📵 ;
J. M. Geria 📵 ; J. J. Bonaparte 📵 ; T. Muscheid 📵 ; R. Gartmann 📵 ; A. Almela 📵 ; M. R. Hampel 📵 ;
A. E. Fuster 📵 ; L. E. Ardila-Perez 📵 ; M. Wegner 📵 ; M. Platino 📵 ; O. Sander 📵 ; S. Kempf 📵 ; M. Weber 📵

🔄 Check for updates

View Online   Export Citation

Articles You May Be Interested In

SLAC microresonator RF (SMuRF) electronics: A tone-tracking readout system for superconducting microwave resonator arrays

Rev. Sci. Instrum. (January 2023)

Note: Innovative demodulation scheme for coherent detectors in cosmic microwave background experiments

Rev. Sci. Instrum. (May 2012)

Frequency-domain multiplexed readout of transition-edge sensor arrays with a superconducting quantum interference device

Appl. Phys. Lett. (March 2005)

Optimal demodulation domain for microwave SQUID multiplexers in presence of readout system noise

View Online   Export Citation   CrossMark

M. E. García Redondo,[1,2,3,4,a)] N. A. Müller,[1,3,4,5] J. M. Salum,[1,2,3,4] L. P. Ferreyro,[1,2,4,6]
J. D. Bonilla-Neira,[1,4,5,6] J. M. Geria,[1,5,6] J. J. Bonaparte,[3,4,5] T. Muscheid,[2] R. Gartmann,[2] A. Almela,[1,3]
M. R. Hampel,[1,3,6] A. E. Fuster,[1,3,6] L. E. Ardila-Perez,[2] M. Wegner,[2,5] M. Platino,[1,3,4,6] O. Sander,[2]
S. Kempf,[2,5] and M. Weber[2]

AFFILIATIONS

[1]Instituto de Tecnologías en Detección y Astropartículas (ITeDA), Buenos Aires, Argentina
[2]Institute for Data Processing and Electronics (IPE), Karlsruhe Institute of Technology (KIT), Karlsruhe, Germany
[3]Comisión Nacional de Energía Atómica (CNEA), Buenos Aires, Argentina
[4]Escuela de Ciencia y Tecnología (ECyT), Universidad Nacional de San Martín (UNSAM), Buenos Aires, Argentina
[5]Institute of Micro- and Nanoelectronic Systems (IMS), Karlsruhe Institute of Technology (KIT), Karlsruhe, Germany
[6]Consejo Nacional de Investigaciones Científicas y Técnicas (CONICET), Buenos Aires, Argentina

[a)]Author to whom correspondence should be addressed: manuel.garcia@iteda.cnea.gov.ar

ABSTRACT

The Microwave SQUID Multiplexer (µMUX) is the device of choice for the readout of a large number of low-temperature detectors in a wide variety of experiments within the fields of astronomy and particle physics. While it offers large multiplexing factors, the system noise performance is highly dependent on the cold- and warm-readout electronic systems used to read it out, as well as the demodulation domain and parameters chosen. In order to understand the impact of the readout systems in the overall detection system noise performance, first, we extended the available µMUX simulation frameworks, including additive and multiplicative noise sources in the probing tones (i.e., phase and amplitude noise), along with the capability of demodulating the scientific data, either in the resonator's phase or the scattering amplitude. Then, considering the additive noise as a dominant noise source, the optimum readout parameters to achieve minimum system noise were found for both open-loop and flux-ramp demodulation schemes in the aforementioned domains. Later, we evaluated the system noise sensitivity to multiplicative noise sources under the optimum readout parameters. Finally, as a case study, we evaluated the optimal demodulation domain and the expected system noise level for a typical software-defined radio readout system. This work leads to an improved system performance prediction and noise engineering based on the available readout electronics and the selected demodulation domain.

I. INTRODUCTION

Low-temperature detectors, such as Transition-Edge Sensors (TESs),[1] Magnetic Microcalorimeters (MMCs),[2] and Microwave Kinetic Inductance Detectors (MKIDs),[3] have demonstrated outstanding sensitivities in a large number of different experiments going from sub-mm/mm[4] and gamma/x-ray[5] astronomy to nuclear and particle physics.[6] Nowadays, current micro- and nano-fabrication techniques allow one to easily create focal planes populated with a huge number of detectors satisfying the requirements of the most demanding applications.[7] At the same time, multiplexing schemes that support these large detector counts are being developed in parallel in order to manage the system complexity and cooling requirements at sub-kelvin stages where the detectors are operated.[8]

Along with the different multiplexing techniques developed for cryogenic detectors readout, a Frequency-Division Multiplexing

(FDM) scheme that has become popular in the last decade is the Microwave Superconducting Quantum Interference Device (SQUID) Multiplexing (μMUXing).[9,10] Its success lies in the available high channel carrying capacity and remarkable system scalability while maintaining the readout noise subdominant to the intrinsic detector noise.[11] This scheme encodes the detector signals in the resonance frequencies of multiple GHz-frequency superconducting resonators coupled to a common feedline. Therefore, recovering the signals from each detector requires only monitoring the resonance frequencies. Despite these advantages, it places stringent requirements on the cold- and warm-readout systems responsible for generating and acquiring high-purity broadband microwave signals required to monitoring each channel.

Particularly for low-detector count experiments with wider bandwidth resonators (e.g., as used for x-ray pulse detection[12]), the readout system noise is mainly dominated by the cryogenic Low-Noise Amplifier (LNA) in charge of recovering the low-power microwave signals coming out of the μMUX device.[13] Contrary, for high-detector count experiments using narrower resonances (e.g., as used for CMB surveys[11]), readout system noise tends to be dominated by the Two-Level System noise (TLS).[10] For the case of single channel in-lab characterization, the conditions in which the system noise is dominated by cryogenic LNA or TLS noise are easily achieved using bench-top instruments and expensive microwave components. This is not the case for *in situ* measurements in either ground-based or space-based experiments. These kinds of experiments usually use custom designed Software-Defined Radio (SDR) readout systems based on commercially available components with limited performance in comparison with bench-top instruments.[14–17] Therefore, the impact of the readout electronics becomes more relevant, especially in the readout of flux-transformer coupled devices, such as magnetic microcalorimeters/bolometers[12,18] or with the introduction of near–quantum-limited amplification technologies, such as parametric amplifiers.[19,20] As a consequence, it is important to have a software simulation framework, which allows designers to predict the impact of these systems on the readout performance, as well as, through its characterization, evaluate the readout parameters that optimize the yield of a particular detection system.

Seeking to improve system noise predictions and find optimization parameters, we extended in this article the capabilities of the available simulation frameworks for the readout of microwave SQUID multiplexers[21,22] allowing one to evaluate the impact of the cold- and warm-readout electronics systems in the overall readout performance. Previously developed frameworks solely consider additive noise, commonly attributed to the cryogenic LNA. However, characterizations performed over SDR readout systems unveil the presence of multiplicative noise.[16,23–25] These extra noise sources were included in the present study, and their impact in the system performance was evaluated as a function of the readout parameters. Since the noise sources added act in different domains, the most commonly used demodulation domains were also included. In order to avoid confusing readers, throughout this document, we will use the term "domain" to refer to the coordinate system where the signal from a single detector is encoded. This term should not be confused with the "space" where the different detectors are multiplexed (e.g., time, frequency, or code). For the case of μMUX, which is a multiplexing device in the frequency space, we will analyze the two most commonly used readout domains according to the available literature. As we will detail later, the two demodulation domains are the amplitude of the transmission scattering parameter γ and the resonator's phase θ. It is important to mention that the scope of this work only considers the readout by a single fixed tone and is not directly applicable to the analysis of other recently proposed readout techniques, such as tone-tracking.[15,21]

This article is organized as follows: First, in Sec. II, we describe the μMUX model used for simulations and its dependence with flux and power. Second, Sec. III presents the readout signal model adding additional noise sources attributed to the readout system, and two demodulation schemes and domains are presented. Then, in Sec. IV, we show through simulations the minimum-noise readout parameters for additive noise in both demodulation schemes and evaluate the impact of the remaining noise sources under these conditions using a variety of different demodulation parameters. In addition, the impact of a typical SDR readout system is analyzed as an example. Finally, a discussion based on the obtained results is given in Sec. V, and the conclusions are presented in Sec. VI.

II. MICROWAVE SQUID MULTIPLEXER MODEL

Evaluating the readout performance of a μMUX under readout system noise first requires a model capable of replicating the complex underlying physics of superconducting resonators combined with the nonlinear behavior of Josephson tunnel junctions. In this section, we introduce the most important aspects of a μMUX model that we will employ in Sec. III. It is worth mentioning that the main objective of this work is not to improve the current μMUX models, but rather to reuse the available ones[22,26] within a new simulation framework that includes new features and noise sources.

μMUXing relies on High-Q superconducting microwave resonators as frequency encoding elements. Figure 1 shows a simplified schematic circuit diagram of a transmission line based μMUX. It comprises a non-hysteretic current-sensing rf-SQUID inductively coupled to a superconducting quarter-wave transmission line resonator. The resonator, in turn, is capacitively coupled to a common feedline. Due to its Josephson parametric self-inductance, the rf-SQUID acts as a flux-dependent inductor allowing the resonance frequency modulation by means of the flux threading the SQUID loop, which is proportional to the detector signal coupled through the detector input coil. As a consequence, a probing tone injected at the multiplexer input (left spectrum in Fig. 1) will appear modulated in phase and amplitude at the multiplexer output (right spectrum in Fig. 1). In this way, demodulating the output tones corresponding to each resonator allows us to decode the detector signals using a single pair of coaxial cables going in and out of the cryostat.

As in communications systems, noise performance in the presented scheme depends on the type of modulation used, signal power, and noise level. Accordingly, we will start describing the modulation produced by the μMUX in the probing tones. In Subsection II A, we will present the resonance frequency flux and
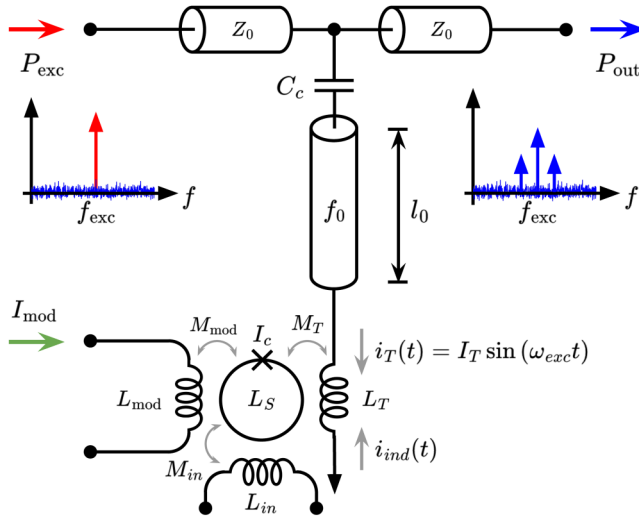
FIG. 1. Simplified schematic circuit diagram of a single readout channel of a transmission line based microwave SQUID multiplexer. (Left) Probing tone spectrum with frequency f_{exc} and power P_{exc}. (Right) Output tone spectrum with its modulation sidebands produced by the μMUX.

power dependence. Then, in Subsection II B, we will relate it with the resonator frequency response and finally in Subsection III C introduce an example model that will be used in Secs. III and IV.

A. Resonance frequency flux and power dependence

For the purpose of this work, we directly adopted the analytical μMUX readout power dependent model developed by Wegner et al.[26] to describe the dependence of the resonance frequency as a function of the fluxes contributions threading SQUID loop $f_r(\varphi)$. This model assumes a finite self-screening parameter $\beta_L = 2\pi L_S I_c/\Phi_0$ as well as a non-zero readout available power P_{exc} at the μMUX input port with angular frequency $\omega_{exc} = 2\pi f_{exc}$. Under this condition, the supercurrent in the rf-SQUID can be written as

$$I_S(t) = -I_c \sin\left[\varphi_{mod} + \varphi_{exc}\sin(\omega_{exc}t) + \beta_L\frac{I_S(t)}{I_c}\right], \quad (1)$$

where $\varphi_{mod} = 2\pi M_{mod}I_{mod}/\Phi_0$ is a quasi-static magnetic flux contribution induced by a current source I_{mod} coupled through M_{mod}, $\varphi_{exc} = 2\pi M_T I_T/\Phi_0$ is the amplitude of the time-variant magnetic flux induced by the probing tone through M_T, and I_c is the critical current of the Josephson junction. The term $\varphi_{scr}(t) = \beta_L I_S(t)/I_c$ represents the self-screening flux. According to Lenz's law, a voltage $u_{ind}(t) = -M_T dI_s(t)/dt$ is created, which opposes the flux changes, and hence, the current $i_{ind}(t)$ is induced in the resonator termination. Therefore, the total current at the resonator termination $i_{tot}(t) = i_T(t) + i_{ind}(t)$ is a superposition of two contributions originating from the microwave probing tone and the supercurrent flowing through the SQUID loop. In this way, the total voltage across the resonator termination is $u_{ind}(t) = L_T di_{tot}(t)/dt$ and can be expressed by

introducing an effective termination inductance,

$$L_{T,eff} = L_T\frac{i_{tot}(t)}{i_T(t)}. \quad (2)$$

Due to the transcendental nature of Eq. (1), there is no analytical solution for $I_S(t)$ than can be directly inserted into Eq. (2). The required approximations and expansions of $I_S(t)$ in order to obtain a useful expression for $L_{T,eff}$ are described by Wegner et al.[26] The derived expression can be directly related to the circuit parameters shown in Fig. 1 yielding to the following resonance frequency expression as a function of the normalized fluxes $f_r(\varphi_{exc}, \varphi_{mod})$:

$$f_r(\varphi_{exc}, \varphi_{mod}) \approx f_{off} + \frac{4f_0^2 M_T^2}{Z_0 L_S}\frac{2\beta_L}{\varphi_{exc}}\sum_{i,j} p_{i,j}(\varphi_{exc}, \varphi_{mod}), \quad (3)$$

where $f_{off} = f_0 - 4f_0^2(C_c Z_0 + L_T/Z_0)$ stands for the unaltered resonance frequency and $p_{i,j} = a_{i,j}\beta_L^{b_{i,j}}J_1(c_{i,j}\varphi_{exc})\cos(c_{i,j}\varphi_{mod})$ are the Taylor expansion coefficients. Here, i denotes the expansion order and j the number of contribution of each order, while J_1 is the order 1 Bessel function of the first kind. It is not the purpose of this article to derive the model equations in detail again, but to give the basic necessary elements to understand Secs. II B and II C. $p_{i,j}$ coefficients, as well as a detailed analysis, can be found in Refs. 26 and 27. The validity of this model sets an upper limit for $\beta_L \leq 0.6$ and assumes a probing tone frequency f_{exc} close to the resonance frequency of the resonator f_r, leading to a maximum oscillating anti-node current amplitude $I_T = \sqrt{\frac{16Q_l^2 P_{exc}}{\pi Q_c Z_0}}$. Q_l and Q_c denote the loaded and coupling quality factors, respectively, while Z_0 is the characteristic impedance of both the resonator and the feedline.

B. Frequency response

The previously introduced expression can be inserted into the resonator transmission scattering parameter in order to find the flux dependence of the resonator frequency response $S_{21}(f_{exc}, \varphi)$. Considering a perfectly symmetric lossy resonator,[22,28] the analytical expression becomes

$$S_{21}(f_{exc}, \varphi_{exc}, \varphi_{mod}) = \frac{S_{21}^{min} + 2jQ_l\left(\frac{f_{exc} - f_r(\varphi_{exc}, \varphi_{mod})}{f_r(\varphi_{exc}, \varphi_{mod})}\right)}{1 + 2jQ_l\left(\frac{f_{exc} - f_r(\varphi_{exc}, \varphi_{mod})}{f_r(\varphi_{exc}, \varphi_{mod})}\right)}. \quad (4)$$

Here, $S_{21}^{min} \approx Q_l/Q_i$ represents the resonance depth and Q_l and Q_i are the loaded and intrinsic quality factors, respectively. This equation describes a Lorentzian shaped frequency response that in the complex plane follows a semi-circular trajectory with a center at $x_c = (1 + S_{21}^{min})/2$ and radius $r = 1 - x_c$ as can be seen in Fig. 2. This trajectory is approximately the same either for flux or frequency sweeps in the case of a negligible junction sub-gap conductance.[12,27] In the case of high quality resonators ($Q_i \rightarrow \infty$), the bandwidth of the resonator can be easily approximated using $BW_{res} \approx f_0/Q_l$. Therefore, $Q_l \approx Q_c$, and BW_{res} is only determined via coupling through C_c. The symmetric frequency response
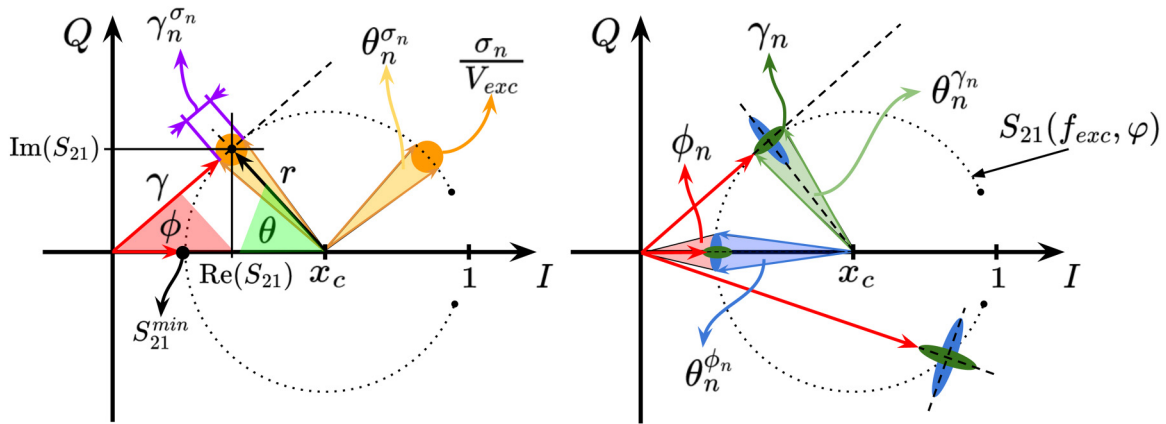
FIG. 2. Complex plane representation of the transmission scattering parameter $S_{21}(f_{exc}, \varphi)$ in its canonical form, with the readout noise sources. Red arrows represent the normalized measured signal phasor with amplitude $\gamma = |S_{21}|$ and phase ϕ, while θ is the resonator's phase measured from its rotating frame. (Left) Additive source: Johnson–Nyquist noise $\sigma_n(t)/V_{exc}$ represented as a circular orange noise cloud. (Right) Multiplicative sources: Phase $\phi_n(t)$ and amplitude $\gamma_n(t)$ noises represented with the blue and green ellipses, respectively. The projection of each noise source into the resonator's phase and scattering amplitude demodulation domains are denoted as $\gamma_n^{\sigma_n}(t)$, $\theta_n^{\sigma_n}(t)$, $\theta_n^{\gamma_n}(t)$, and $\theta_n^{\phi_n}(t)$. The superscript stands for the noise source that is being projected.

described by Eq. (4) is a consequence of a good impedance matching between the resonator and the associated feed-line.[27,28]

C. μMUX simulation example

The μMUX analytical model described by Eqs. (3) and (4) was numerically implemented using Python and tested with device parameters described in Table I, which are typical for a μMUX device used in bolometric applications.[11] Using Eq. (3), the unaltered resonance frequency was calculated yielding $f_{off} = 4.775$ GHz, while the peak-to-peak frequency shift Δf_r^{mod} for vanishing readout powers $P_{exc} \to 0$ matches the resonator bandwidth $BW_{res} \approx 200$ kHz. Since we commonly place the probing tone frequency f_{exc} close to the unaltered resonant frequency f_{off}, it is more convenient to express it in terms of the difference $f_{exc} - f_{off}$ instead of its absolute frequency. We adopted this metric for our graphs in this work. Accordingly to the analytical model predictions at a power around $P_{exc} \approx -64$ dBm,

TABLE I. μMUX example parameters used during simulations. These are the typical design parameters for a μMUX optimized for bolometric applications.[11]

Parameter	Value	Unit
f_0	5	GHz
Z_0	50	Ω
L_S	30	pH
L_T	100	pH
β_L	0.6	…
M_T	1.3	pH
M_{mod}	20	pH
Q_i	200 000	…
C_c [a]	5	fF

[a]$Q_c \approx (2\pi)/(2\, Z_0 \omega_0\, C_c)^2$.

the resonator became insensitive to the modulation flux φ_{mod}. For this reason, simulations performed in this work were limited to a power range between -90 and -60 dBm.

It should be noted that the required condition of a probe tone frequency f_{exc} being as close as possible to the resonance frequency f_r cannot be always satisfied, yielding to an overestimation of the radio-frequency flux induced within the SQUID when the probing tone is far away from it. In this case, an analytical calculation of $I_T(f_{exc})$ cannot be found due to the recursive relation between $f_r(\varphi_{exc})$ and $\varphi_{exc}(f_r)$. Therefore, we applied a similar solution that was used in previous articles.[22] However, in this case, the maximum value of the anti-node current $I_T = \sqrt{\frac{16 Q_l^2 P_{exc}}{\pi Q_c Z_0}}$ was scaled using narrow-band approximation of the transmission line resonator frequency response given by expression (4). This iterative process starts at a zero readout power condition $P_{exc} \to 0$ to derive a first guess $f_r^{i=0}$ and then executes the power dependent model sequentially using the previous results f_r^{i-1} until the equilibrium is reached, or equivalently, the convergence criteria is satisfied $f_r^{i-1} \approx f_r^i + \epsilon$.

Due to the fact that in Sec. III, we use a continuous-time analytical description, and time-dependency was introduced considering a time varying modulation flux $\varphi_{mod}(t)$. The quasi-static flux condition imposed for Eq. (1) is fulfilled ensuring flux variations considerably slower than the resonator ringdown time $\tau_{down} \approx 1/2\pi BW_{res}$ and consequently even slower than $\tau_{exc} = 1/2\pi f_{exc}$. This condition allowed the resonator to keep track of the flux variations while maintaining the steady-state frequency response[22,29] described by Eq. (4). Nevertheless, our model allows us to calculate a first order approximation of the dynamic response by means of a low-pass filtered version of S_{21}. In order to simplify the nomenclature and facilitate the following analysis, we will only show explicitly the time dependence of the transmission parameter $S_{21}(t)$ as a consequence of the flux variations $\varphi(t)$.
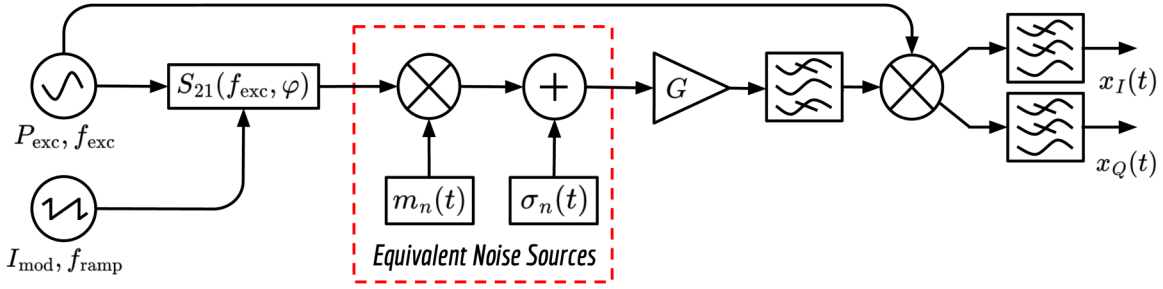
FIG. 3. Block diagram of the homodyne readout system used for the readout of a microwave SQUID multiplexer. From left to right) Microwave and arbitrary signal generators in charge of generating the probing tone and flux modulation, µMUX device, equivalent noise sources, low-noise amplifiers, filters, and the IQ mixer for signal conditioning and downconversion. The noise sources inside the red rectangle $\sigma_n(t)$, $m_n(t)$ represent the additive and multiplicative noise sources attributed to the cold- and warm-readout system, respectively, and referred to the µMUX output.

III. READOUT SYSTEM MODEL

A simplified block diagram of the homodyne system used for the readout of a single µMUX channel is shown in Fig. 3. For the sake of simplicity, several of the microwave/RF components comprising the cold- and the warm-temperature electronics were condensed into single blocks while preserving its functionality. The most important components of this system are (1) A microwave synthesizer capable of generating the probing tone with frequency f_{exc} and available power P_{exc} at the µMUX input port, (2) an arbitrary current waveform generator able to provide the required flux modulation φ_{mod} with frequency f_{ramp}, (3) the µMUX device described by the behavioral model explained in Sec. II, (4) a set of noise sources representing all noise contributions attributed to the readout system (dashed red box), (5) low-noise amplification and filtering stages in charge of boosting the signals and filtering out unwanted components maintaining the Signal-to-Noise Ratio (SNR), and (6) a complex IQ mixer that downconverts the signal in order to be processed later.

A. Measured signals and noise sources

The complex base-band signal $x(t) = x_I(t) + jx_Q(t)$ at the output of the homodyne readout system shown in Fig. 3 can be expressed as

$$x(t) = G'V_{exc}S_{21}(t)m_n(t) + G'\sigma_n(t), \qquad (5)$$

where $V_{exc} = \sqrt{2P_{exc}Z_0}$ is the amplitude of the probing tone, while $\sigma_n(t)$ and $m_n(t)$ are the additive and multiplicative noise terms, respectively. Here, we consider an ideal IQ mixer and a gain factor $G' = G\,e^{j\alpha}\,e^{2j\pi f_{exc}\tau}$, including the overall gain G, phase offset α, and time delay τ added by the RF components and cables. In the context of a real measurement, G' can be determined during the calibration process or continuously monitored.[30] Therefore, for the purpose of this article, we will assume that all of the aforementioned parameters are known and constant over time for the probing tone frequency f_{exc}. During the downconversion process, the time dependence of the excitation signal was removed keeping only the complex envelope of the modulated probing tone being

equal to the scaled transmission parameter time-trace $G'S_{21}(t)$. When f_{exc} is located out of resonance, the transmission parameter is close to unity and the measured average signal amplitude is approximately equal to $x^{off}(t) \approx G'V_{exc}$. This value can be used to define a normalized signal as

$$\frac{x(t)}{x^{off}(t)} = S_{21}^{meas}(t) = S_{21}(t)m_n(t) + \frac{\sigma_n(t)}{V_{exc}}. \qquad (6)$$

Thus, the normalized signal is basically an estimation of the actual transmission parameter $S_{21}(t)$. Figure 2 shows the complex representation of S_{21}^{meas} where, as we mention in Sec. II B and for the noise-less case, the measured signal (red arrow) describes a semi-circle centered at x_c with radius r as a consequence of a flux sweep. The $|S_{21}^{meas}|$ takes values from S_{21}^{min} on resonance to $S_{21} \approx 1$ far out of resonance. Contrarily, in a real scenario represented by Eq. (5), noise sources produce a deviation from this trajectory that cannot be distinguished from the flux variations produced by the detector signal and are interpreted as a flux noise. In Subsections III A 1 and III A 2, we give a detailed description of the noise sources affecting the system in order to calculate the error in the transmission parameter determination and consequently derive the equivalent flux noise represented by each one. Since we want to analyze the impact of the readout system noise over different demodulation domains, we did not consider a detector, SQUID, and modulation flux noise sources.

1. Additive sources

This type of noise refers to all kinds of noise sources that are directly added to the desired signals and remain even if the desired signal is not present. Considering the scope of this work, and based on previous articles,[20,22] we will only consider Johnson–Nyquist noise $\sigma_n(t)$. Johnson–Nyquist noise can be modeled as $\sigma_n(t) = \sigma_I(t) + j\sigma_Q(t)$, where real and imaginary components are both zero-mean, finite power, Independent and Identically Distributed (IID) Gaussian random variables. A normalized version $\sigma_n(t)/V_{exc}$ can be seen as an orange circular noise cloud in Fig. 2. This model is well suited to describe a wide range of noise

sources present in readout electronics systems, such as thermal, electric, or quantization. In a properly designed system, the additive noise is typically dominated by the cryogenic High-Electron Mobility Transistor (HEMT) amplifier.[31] Because of their importance, many groups are actively trying to improve them or even replace them with new amplification technologies, such as quantum-limited parametric amplifiers.[19,20] While these new technologies represent an important reduction of the additive noise level, they make evident the presence of other types of sources such as those we describe below. Additionally to the Johnson–Nyquist noise, spurious signals generated by the electronics[16] can also be included as additive interferences, but for the scope of this work, they will not be included because unlike noise, they are localized in frequency and can be separately mitigated.[32]

2. Multiplicative sources

Contrary to additive sources, multiplicative noise sources depend on the presence of the desired signal. Their level depends on the signal strength, and mathematically, as the name implies, the noise is multiplied to the desired signal $S_{21}(t)$ as

$$m_n(t) = [1 + \gamma_n(t)]\, e^{j\phi_n(t)}. \tag{7}$$

Here, we will only focus on amplitude $\gamma_n(t)$ and phase $\phi_n(t)$ noise. These are the most common multiplicative noise sources present in readout electronics systems.[33,34] Both are real random variables described by their auto-correlation function as we will explain in Subsection III B. A simplified and magnified representation of these noises using colored ellipses is shown in the right side of Fig. 2. The term $\gamma_n(t)$ represents small signal variations (green ellipses) parallel to the measured signal amplitude (red arrow), while $\phi_n(t)$ as perpendicular signal variations (blue ellipses). Due to their multiplicative nature, when the measured signal amplitude decreases (i.e., at resonance), the voltage fluctuations decrease proportionally keeping the amplitude and phase variations constant. Traditionally, amplitude and phase noise are terms used to describe short-term variations or instabilities, with "short-term" referring to time intervals on the order of seconds or less.[35] These are commonly generated when some system parameter randomly fluctuates (e.g., due to thermal or flicker noise) translating that variation to the desired signal. This process called parametric upconversion does not differ too much from the μMUX working principle where the resonance frequency (system parameter) is modulated proportionally to the detector signal. This is the reason why the interest of this work is focused on including these noise sources and evaluating their impact on the system noise.

Besides being focused on noise sources generated by the readout system, this paper additionally includes the two-level system noise. The evidence suggests that this noise is caused by Fluctuating Two-Level Systems (TLSs) in dielectric materials, either the bulk substrate or its exposed surface, the interface layers between the metal films and the substrate, or any oxide layers on the metal surfaces that comprises the transmission line resonator.[36,37] This noise affects the distributed capacitance and, therefore, produces fluctuations in the resonance frequency that are seen as rotations of the resonance circle around its center. As well as

amplitude noise in Eq. (7), it can be expressed as frequency fluctuations $f_r \cdot f_{TLS}(t)$ around the unaltered resonance frequency f_{off},

$$f_r(t) = f_r[1 + f_{TLS}(t)]. \tag{8}$$

Although TLS noise is not generated by the readout electronics, it can act differently depending on the demodulation domain and readout parameters as well as the readout noise sources. This is why its impact will also be evaluated.

B. Noise metrics

Due to its random nature, noise is analyzed as a stochastic process. For wide-sense-stationary and ergodic random process $y(t)$, the Wiener–Khinchin theorem says that a power spectral density can be defined in terms of the Fourier transform of the statistical expected value, e.g., the auto-correlation[33] function as follows:

$$S_y(\Delta f) = \mathscr{F}\{R_{yy}(\tau)\} = \mathscr{F}\{\langle y(0), y(\tau)\rangle\}. \tag{9}$$

Thus, spectral features of noise are entirely determined by the Noise Spectral Density $S_y(\Delta f)$ (NSD). The requirement that noise be stationary and ergodic is the equivalent of "repeatable" and "reproducible" in experimental physics. In our case, $S_y(\Delta f)$ is the base-band representation of the NSD measured at a frequency offset Δf from the probing tone frequency f_{exc}. For the case of Johnson–Nyquist noise, the statistic independence implies white noise with constant NSD equals to $S_N = k_B T_n$, where T_n is the so-called noise temperature and k_B is Boltzmann's constant. Therefore, the NSD of the normalized Johnson–Nyquist noise respect to the probing tone amplitude $\sigma_n(t)/V_{exc}$ is

$$S_\sigma(\Delta f) = \frac{k_b T_n}{P_{exc}}. \tag{10}$$

This quantity is usually expressed in dBc/Hz and T_n is the noise equivalent temperature referred to the μMUX output. In the context of this work, we will distinguish between T_n and T_{sys} due to the fact that T_{sys} is commonly experimentally determined and as we will see later corresponds to an equivalent noise temperature that takes into account all the different noise sources acting simultaneously and producing the same system noise level.[20]

On the other hand, amplitude, phase, or TLS noise exhibits a certain degree of correlation between realizations yielding to colored noise spectral densities. They are commonly described by a power law, such as

$$S_y(\Delta f) = \sum_n b_n(\Delta f)^n. \tag{11}$$

With values of $n = [-4, 0]$ for phase, $n = [-2, 0]$ for amplitude,[33] and $n = [-1, -1/2]$ for TLS.[36] As in the case of Johnson–Nyquist, phase and amplitude noise are expressed in dBc/Hz and represent the noise power integrated in a 1-Hz bandwidth at a Δf offset from f_{exc} relative to the probe tone power. The TLS is expressed as fractional frequency fluctuations $S_{f_r}(f)/f_r^2$ in

units of Hz^{-1}. Contrary to an uncorrelated source case, depending on the degree of correlation, noise can be removed. This is the case of phase noise in radio systems, which use different oscillators and clocks locked to the same frequency reference during up- and downconversion processes as well as during generation and sampling. Therefore, $\phi_n(t)$ used in Eq. (7) stands for the so-called residual phase noise.[34] Due to the fact that it is a multiplicative quantity, it can be arbitrarily referred to any part of the circuit yielding the same behavior.

C. Readout system example

As an example, Fig. 4 shows residual amplitude and phase noise spectral densities for a Direct-RF Software-Defined Radio (SDR) readout system based on the RFSoC ZCU216 evaluation kit.[38] These measurements were taken at a frequency of $f_{exc} = 5$ GHz using a loop-back cable connecting transmitter (Tx) and receiver (Rx) ensuring that most of the coherent noise is removed in the downconversion/sampling process.[16] In a single measurement at constant power, additive and multiplicative noises cannot be distinguished since both contribute to phase and amplitude noise. In order to separate the two contributions, a power sweep was performed until the amplitude and phase spectra reached power-independent values consistent with the description of the multiplicative noise. A more detailed description of the noise characterization process and the measurement setup is given in Appendix A. The obtained results show that for frequency offsets below 10 kHz amplitude $S_\gamma(\Delta f)$ and phase $S_\phi(\Delta f)$, noise densities have -10 dB/decade slopes demonstrating the colored behavior described by Eq. (11). In the case of amplitude noise, its frequency
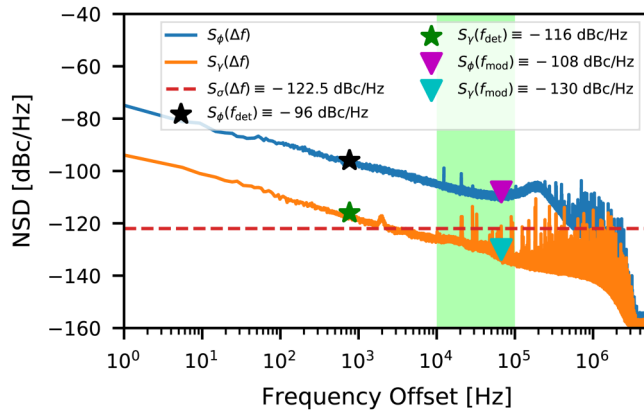
FIG. 4. Noise spectral densities for typical cold- and warm-temperature readout systems at a frequency of $f_{exc} = 5$ GHz. Blue and orange solid lines are the residual phase and amplitude noise spectral densities. The dashed red line is the additive NSD calculated with Eq. (10) using an equivalent noise temperature of a $T_n = 4$ K and probing power $P_{exc} = -70$ dBm. Black and green stars represent phase and amplitude noise measured at $f_{det} \approx 762$ Hz. The green region covers the possible modulation frequencies f_{mod} where the signal of interest is typically located in the case of bolometric applications.[16] Particularly, we used $f_{mod} \approx 62$ kHz, where phase and amplitude noise take values represented by magenta and cyan triangles, respectively.

dependence decays as $1/f$ until it reaches the 1.6 MHz roll-off of the low-pass filter applied during signal channelization. Conversely, in the case of phase noise, for frequency offsets above 10 kHz, it reaches a plateau at around ≈ 200 kHz, where the closed-loop gain of the Phase-Locked Loop (PLL) strongly attenuates the phase noise. This plateau is produced by the noise of the Voltage-Controlled Oscillator (VCO) present in the synthesizer's PLL.[39] Appendix B provides a detailed analysis of the noise sources involved in the synthesis of the sampling clocks, to which the excess phase noise is attributed. In contrast to the multiplicative sources, the additive noise spectral density that is expected to be dominated by the cold-readout system was theoretically calculated using Eq. (10). As an example, for a typical cryogenic LNA with $T_n = 4$ K and assuming a probing power $P_{exc} = -70$ dBm, the additive noise spectral density yields $S_\sigma(\Delta f) \approx -122.5$ dBc/Hz. The noise values shown in Fig. 4 will be used in the Sec. IV along with the µMUX model (Table I) to estimate the readout noise performance for this particular example. These noise values were measured at detector $f_{det} \approx 762$ Hz and modulation frequencies $f_{mod} \approx 62$ kHz and represented with black and green stars and magenta and cyan triangles in Fig. 4.

After all noise sources and metrics were introduced and an example was given, the error term in the determination of the transmission scattering parameter as a function of time $S_{21}(t)$ can be written as

$$\delta S_{21}(t) = S_{21}(t)\gamma_n(t)\,e^{j\phi_n(t)} + \frac{\sigma_n(t)}{V_{exc}}. \quad (12)$$

In Sec. III D, we will introduce the two most widely used demodulation domains and analyze the projection of the error term $\delta S_{21}(t)$ on them in order to evaluate the demodulation performance.

D. Demodulation domains and schemes

Slow variations in the flux, given either by modulation $\varphi_{mod}(t)$ or detector $\varphi_{det}(t)$, lead to variations of the resonator frequency response as described by Eq. (4) and depicted in Fig. 2. The most widely used domains in which these variations are demodulated are (1) the resonator's phase measured from its rotating frame[20,40,41] and (2) the amplitude of the transmission scattering parameter.[22,42] Both are respectively defined as

$$\theta(f_{exc}, \varphi) = \arctan\left\{\frac{\mathrm{Im}[S_{21}(f_{exc}, \varphi)]}{x_c - \mathrm{Re}[S_{21}(f_{exc}, \varphi)]}\right\}, \quad (13)$$

$$\gamma(f_{exc}, \varphi) = |S_{21}(f_{exc}, \varphi)|. \quad (14)$$

The arbitrary selection of these two domains is based on the most commonly used demodulation types according to the literature and the availability of experimental results to validate the results of our simulations.[20,22] A representation of both domains is shown at the left of Fig. 2. While both domains are used showing outstanding performance, there is not an available simulation framework that allows one to compare their performance in the presence of readout system noise, especially multiplicative.

TABLE II. Spectral densities of additive and multiplicative noise sources projected in both demodulation domains. S_θ represents the flux spectral density in resonator's phase readout while S_γ in a scattering amplitude. The dependence of the parameters with f_{exc}, φ, and Δf was removed in order to avoid a complex notation.

Readout domain	Additive noise σ_n	Amplitude noise γ_n	Phase noise ϕ_n
S_θ	$\frac{1}{r^2}\frac{k_b T_n}{P_{exc}}$	$\frac{\gamma^2 \sin^2(\phi+\theta)}{r^2}S_\gamma$	$\frac{\gamma^2 \cos^2(\phi+\theta)}{r^2}S_\phi$
S_γ	$\frac{k_b T_n}{P_{exc}}$	$\gamma^2 S_\gamma$	...

Using Eqs. (13) and (14), we are able to define the projection of the error term $\delta S_{21}(t)$ in both domains. Thus, $\theta_n^{\sigma_n}(t)$, $\gamma_n^{\sigma_n}(t)$ correspond to resonator-phase and scattering-amplitude error due to additive noise $\sigma_n(t)$, while $\theta_n^{\phi_n}(t)$ and $\theta_n^{\gamma_n}(t)$ correspond to the resonator's phase error due phase $\phi_n(t)$ and amplitude $\gamma_n(t)$ noise, respectively. Unlike the rest, amplitude noise $\gamma_n(t)$ is already projected into the scattering amplitude domain by definition. These projections are depicted in Fig. 2 using shaded yellow, green, red, and blue triangles. In the condition of small noise amplitudes, the geometrical projection of each noise source into the different domains can be calculated and the NSD derived yielding the analytical expressions shown in Table II. A detailed analysis of these derivations is found in Appendix C. The dependence of the NSD with f_{exc}, φ, and Δf was removed in order to avoid a complex notation.

Expressions in Table II corresponding to additive noise represent the easiest cases to analyze because they describe a constant radius noise cloud independent of the trajectory described by the resonator's response. Therefore, its projections either in a resonator's phase or a scattering amplitude are constant. Conversely, multiplicative noise projections depend on the position in the resonance circle $S_{21}(f_{exc}, \varphi)$ in which they are calculated (i.e., scattering amplitude γ, scattering phase ϕ, and resonator's phase θ). Particularly, in these cases, there can be a condition for minimum or zero projection depending on the readout domain and readout parameters chosen. For example, in the case of readout amplitude noise $\gamma_n(t)$, there is no projection onto the resonator's phase domain when the readout phasor (red arrow in Fig. 2) is parallel to the circle radius ($\theta + \phi = 0$). In contrast, for readout phase noise $\phi_n(t)$, there is no projection onto the resonator's phase domain when the readout phasor is tangent to the resonance circle ($\theta + \phi = \pi/2$). In addition, using the expressions in Table II, we conclude that additive noise is the dominant noise due to the fact that, when considering equal noise densities (i.e., $S_\gamma = S_\phi = \frac{k_b T_n}{P_{exc}}$), multiplicative sources are scaled by factors lower than unity with respect to the additive. Despite these expressions allowing us to calculate the resonator's phase and scattering amplitude noise projections, an additional step is required in order to convert them to flux noise for a later comparison. This step depends on the demodulation scheme used and will be explained below.
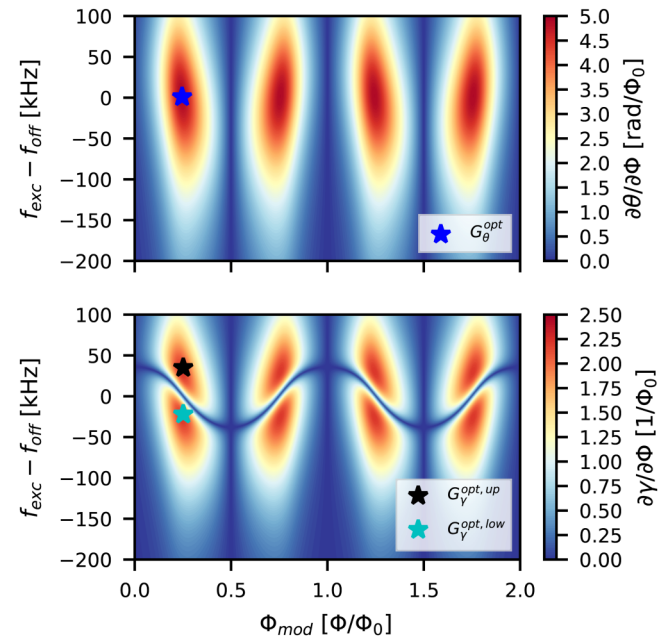
1. Open-loop demodulation

When a detector signal is coupled to the SQUID through the input coil L_{in} (see Fig. 1), it creates a flux component $\varphi_{det}(t)$ that is added to the modulation flux $\varphi_{mod}(t)$. For a given constant f_{exc}, and flux φ_{mod}, small flux variations $\delta\varphi_{det}(t)$ will lead to resonator's phase $\theta(t)$ and scattering amplitude $\gamma(t)$ variations described by

$$\theta(t) \approx \delta\varphi_{det}(t)\left.\frac{\partial\theta}{\partial\varphi}\right|_{f_{exc},P_{exc},\varphi_{mod}}, \tag{15}$$

$$\gamma(t) \approx \delta\varphi_{det}(t)\left.\frac{\partial\gamma}{\partial\varphi}\right|_{f_{exc},P_{exc},\varphi_{mod}}. \tag{16}$$

This readout scheme is called an open-loop, and the demodulated signals $\theta(t)$ and $\gamma(t)$ are scaled copies of $\delta\varphi_{det}(t)$. The scaling factors are denoted as open-loop gains or transfer coefficients equivalently, being equal to the partial derivatives of the corresponding demodulation domain with respect to the normalized flux evaluated at f_{exc}, P_{exc}, and φ_{mod}. Consequently, the maximum demodulated signal amplitudes are obtained when the maximum partial derivatives are achieved. Figure 5 shows the simulated resonator's phase (top) and scattering amplitude (bottom) derivatives for the μMUX model described in Sec. I as a function of the modulation flux φ_{mod} and probing tone frequency f_{exc} for a specific probing power $P_{exc} = -70$ dBm. The absolute maximum gain for the resonator's phase G_θ^{opt} is represented by the blue star, while

FIG. 5. Open-loop gains corresponding to the μMUX model presented in Table I as a function of probe frequency f_{exc} and modulation flux φ_{mod} for a constant probing power $P_{exc} = -70$ dBm. (top) Resonator's phase gain—blue star represents the maximum gain G_θ^{opt}. (bottom) Scattering amplitude gains—black and cyan stars represent both upper $G_\gamma^{opt,up}$ and lower $G_\gamma^{opt,low}$ local maximum gains.

upper $G_\gamma^{opt,up}$ and lower $G_\gamma^{opt,low}$ local maximum open-loop gains with black and cyan stars, respectively.

These gain factors allow us to calculate the resonator's phase and scattering amplitude variations but can also be used in the reverse way to derive the equivalent flux change for given resonator phase and amplitude variations. Therefore, the NSD of the noise projections listed in Table II can be translated into an equivalent flux noise density for resonator's phase $\sqrt{S_\Phi^\theta}$ and scattering amplitude $\sqrt{S_\Phi^\gamma}$ readout using

$$\sqrt{S_\Phi^\theta} \approx \sqrt{S_\theta(\Phi)} \left| \frac{\partial\theta(\Phi)}{\partial\Phi} \right|^{-1}, \qquad (17)$$

$$\sqrt{S_\Phi^\gamma} \approx \sqrt{S_\gamma(\Phi)} \left| \frac{\partial\gamma(\Phi)}{\partial\Phi} \right|^{-1}. \qquad (18)$$

Simplifying the notation for reading purposes, the dependence of the noise projection with probing frequency and power was avoided only by preserving the explicit dependence with the magnetic flux Φ. A similar expression for the flux noise $\sqrt{S_\Phi^{TLS}}$ can be found for TLS noise.[10,27] Since it acts directly in the resonance frequency, it can be related to the flux using

$$\sqrt{S_\Phi^{TLS}} \approx \sqrt{S_{f_r}} \left| \frac{\partial f_r(\Phi)}{\partial\Phi} \right|^{-1}, \qquad (19)$$

where $\frac{\partial f_r(\Phi)}{\partial\Phi}$ is the derivative of Eq. (3) with respect to the flux and $\sqrt{S_{f_r}}$ the frequency NSD. Although it is experimentally possible to determine the optimum flux bias necessary to obtain the maximum transfer coefficients, one of the main disadvantages of this scheme is that the information lies in the modulation sidebands located at a frequency offset equal to f_{det}, where generally, the phase $S_\phi(f_{det})$, amplitude $S_\gamma(f_{det})$, and TLS $S_{f_r}(f_{det})$ noise sources are considerably larger compared to the Johnson–Nyquist noise $\frac{k_B T_n}{P_{exc}}$, as it can be seen in Fig. 4 represented with green and black stars. Therefore, special care should be given to multiplicative and TLS noise sources in the case of bolometric applications where the detector signal is extremely slow and faint,[11,18] or a different readout method to overcome this problem has to be used.
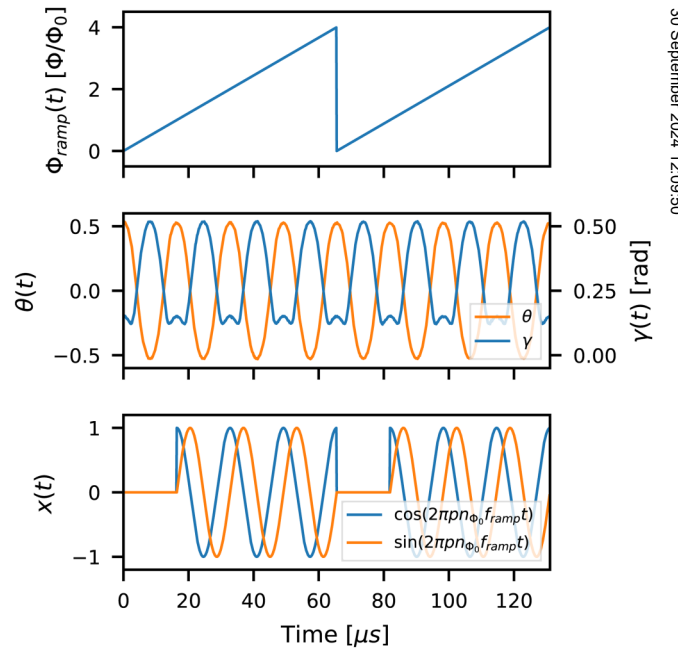
2. Flux-ramp demodulation

In addition to the aforementioned problem, random flux offsets trapped inside the SQUID loop would require individual flux tuning of every channel in order to achieve the maximum open-loop gain, re-introducing the multiplexing problem. A technique called Flux-Ramp Modulation[29] (FRM) was introduced as a solution to overcome this limitation. In this technique, a common flux line is shared among all SQUIDS and a sawtooth-shaped flux with amplitude $M_{mod}I_{mod} = n_{\Phi_0}\Phi_0$ and reset frequency f_{ramp} being applied sweeping all the possible operating points (see the upper plot in Fig. 6). Due to the SQUID periodic response, resonator's phase $\theta(t)$ and scattering amplitude $\gamma(t)$ will have the same periodicity equal to $f_{mod} = n_{\Phi_0}f_{ramp}$. Therefore, a considerably slow detector signal $\varphi_{det}(t)$ added to the sawtooth-shaped modulation can be

seen as a phase modulation, where $\varphi_{det}(t)$ determines the instantaneous phase changes of the periodic responses (the middle plot in Fig. 6). As a consequence of FRM, the detector signal is upconverted to the frequency $f_{mod} = n_{\Phi_0}f_{ramp}$ (the green region in Fig. 4) avoiding in this way noise levels close to the probe tone frequency f_{exc}. However, an additional phase demodulation step is required in order to recover the detector signal (Flux-Ramp Demodulation or FRD). In the context of this article, we will analyze the flux demodulation noise performance using the linearity-improved quadrature demodulation.[43] The demodulated flux for the resonator's phase $\theta(t)$, and scattering amplitude $\gamma(t)$, demodulation can be written, respectively, as

$$\varphi_\theta(t') = \arctan\left[\frac{\int \sin(2\pi p f_{mod} t) w(t) \theta(t)\, dt}{\int \cos(2\pi p f_{mod} t) w(t) \theta(t)\, dt} \right], \qquad (20)$$

$$\varphi_\gamma(t') = \arctan\left[\frac{\int \sin(2\pi p f_{mod} t) w(t) \gamma(t)\, dt}{\int \cos(2\pi p f_{mod} t) w(t) \gamma(t)\, dt} \right]. \qquad (21)$$

Here, $w(t)$ accounts for both the discarding window, where a number of SQUID periods n_{disc} is set to zero avoiding the sawtooth-shaped flux non-ideal transition and the window function used to attenuate the non-linearity components. An integer number p is added allowing the demodulation of higher order

FIG. 6. Signals associated with the flux-ramp demodulation process of the μMUX model presented in Table I for a particular f_{exc} and P_{exc}. (top) Flux-ramp modulation signal spanning $n_{\Phi_0} = 4$ with $f_{ramp} \approx 15.25$ kHz. (middle) Resonator's phase and scattering amplitude signals before FRD. (bottom) Reference signals used for demodulation, including the discarded period $n_{disc} = 1$ and using the first harmonic component $p = 1$.

FRM harmonics as we will use later in Sec. IV B 1. The bottom part of Fig. 6 shows the cosine and sine reference signals used for FRD. Particularly, in this example, one of a total of four periods is discarded and a boxcar window is used. In this scheme, the integration is performed over a flux-ramp period setting an effective sampling rate of f_{ramp}. Here, we use continuous-time notation for explanatory purposes and t' to explicitly show this implicit decimation.

In contrast to open-loop demodulation, FRM sweeps all the possible flux values varying the open-loop gains from its maximum and minimum values. As a consequence, Eqs. (18) and (17) need to be integrated over a one flux-ramp period in order to get the demodulated noise level. As a natural solution, a gain-weighted average noise value may be used, but expressions (17)–(19) diverge in the case of zero gain. Due to this, traditionally, a Root-Mean-Square (RMS) gain over a flux-ramp period is defined,[22,29] and the flux noise density in the case of resonator's phase and scattering amplitude is calculated using

$$\sqrt{S_\Phi^\theta} \approx \sqrt{S_\theta} \left\{ \frac{1}{n_{\Phi_0}\Phi_0} \int_{n_{disc}\Phi_0}^{n_{\Phi_0}\Phi_0} \left(\frac{\partial\theta(\Phi)}{\partial\Phi} \right)^2 d\Phi \right\}^{-\frac{1}{2}}, \quad (22)$$

$$\sqrt{S_\Phi^\gamma} \approx \sqrt{S_\gamma} \left\{ \frac{1}{n_{\Phi_0}\Phi_0} \int_{n_{disc}\Phi_0}^{n_{\Phi_0}\Phi_0} \left(\frac{\partial\gamma(\Phi)}{\partial\Phi} \right)^2 d\Phi \right\}^{-\frac{1}{2}}. \quad (23)$$

Similarly, for TLS, a flux noise density can be calculated as well,

$$\sqrt{S_\Phi^{TLS}} \approx \sqrt{S_{f_r}} \left\{ \frac{1}{n_{\Phi_0}\Phi_0} \int_{n_{disc}\Phi_0}^{n_{\Phi_0}\Phi_0} \left(\frac{\partial f_r(\Phi)}{\partial\Phi} \right)^2 d\Phi \right\}^{-\frac{1}{2}}, \quad (24)$$

where expressions between brackets are the gain-mean squares over a flux-ramp period and S_θ, S_γ, and S_{TLS} are evaluated at f_{mod}. Due to the fact that we are discarding n_{disc} periods from a total of n_{Φ_0} and applying a window function, we expect a degradation equal to $\sqrt{\kappa/\alpha}$, where $\alpha = (n_{\Phi_0} - n_{disc})/n_{\Phi_0}$. A κ factor was added to account for the degradation caused by the window applied. When a boxcar window is used, $\kappa = 1$. While these expressions give a rough estimation of the noise level, they have several limitations that this work aims to overcome. Unlike additive and TLS noise, these expressions do not apply to the case of multiplicative noise where both spectral densities and gains are flux dependent (i.e., $\sqrt{S_{\theta,\gamma}(\Phi)}$). Another limitation is that, due to the non-sinusoidal resonator's phase and scattering amplitude responses, the information is not only contained in a single sideband, but spread out in harmonics of f_{mod}, which cannot be demodulated using the quadrature demodulation method. Additionally, an extra challenge lies in the analytical calculation of the derivatives with respect to the flux for the given conditions of readout power and frequency using the model presented in Sec. II and their integration over a flux-ramp period. This is remarkable especially when multidimensional optimization criteria must be found. That is why in this work, the evaluation of the optimal readout parameters that match the lowest

noise condition in both domains and demodulation methods will be performed by means of numerical simulations.

IV. SYSTEM NOISE SIMULATION

In this section, we present several simulations performed in order to evaluate the demodulated noise for different readout conditions. Previously, for sake of simplicity, a continuous-time signal model of the readout system was introduced. From now on, we will migrate to its discrete-time equivalent using adequate sampling frequency f_s that satisfies the sampling theorem. This migration is not only motivated by the numerical simulation, but also because the demodulation is typically done in the digital domain using Software-Defined Radio (SDR) Systems.[15,40,42,44] The readout system simulation framework was implemented completely in Python and making use of several available libraries. Table III enumerates the parameters used in the following simulations.

The general simulation procedure to obtain a demodulated signal time-trace can be summarized as follows:

1. The total modulation flux $\varphi_{tot}[m]$ is created adding the modulation flux $\varphi_{mod}[m]$ to the detector flux $\varphi_{det}[m]$.
2. Given fixed f_{exc} and P_{exc}, $f_r[m]$ is iteratively calculated using Eq. (3) and $f_{TLS}[m]$ is added.
3. $S_{21}[m]$ is calculated using Eq. (4) for a particular f_{exc}, low-pass filtered, and the readout noise sources $\sigma_n[m]$, $\phi_n[m]$, and $\gamma_n[m]$ are included.
4. Finally, and after a new step of signal conditioning, $\theta[m]$ and $\gamma[m]$ are available to be demodulated using some of the methods presented in Sec. III D.

Throughout the simulations presented in this section, some simplifications were adopted. SDR systems exhibit additive and multiplicative noise levels dependent on the attenuation or gain required to obtain the desired probing tone power levels P_{exc} at the μMUX input or the appropriate signal levels at the receiver input. In order to simplify the analysis, we will assume that both the additive and multiplicative noise levels shown in Fig. 4 (i.e., T_n, S_ϕ, and S_γ) are constant over the power range in which the simulations were performed. Although these simplifications are not applicable to all SDR systems, they are applicable to the case of the SDR system characterized in the Appendix A.

TABLE III. Readout system parameters used during demodulated noise simulations.

| Parameter	Value	Unit
f_s	≈7.82	MHz
N_s	2^{20}	Samples
$BW_{readout}$	2	MHz
f_{det}	≈762.90	Hz
A_{det}	1	$m\Phi_0$
f_{ramp}	≈15.25	kHz
n_{Φ_0}	4	…
n_{disc}	1	…
p	1	…
$w[n]$	Hamming	…

A. Open-loop demodulation noise performance

Using our simulation framework, we replicated the measurement process that is carried out in the laboratory during characterization. This allowed us to not only evaluate the noise performance, but also to know the required functionalities of our SDR readout system. For the determination of the noise density in the open-loop scheme described by Eqs. (17) and (18), we must know the value of the open-loop gains (transfer coefficients), which depend on the readout frequency f_{exc} and power P_{exc} as well as the applied constant modulation flux φ_{mod}. First, for each value of frequency and power, one period of the transmission scattering parameter $S_{21}(f_{exc}, P_{exc}, \varphi_{mod})$ was calculated sweeping φ_{mod}. Then, we get resonator's phase $\theta(f_{exc}, P_{exc}, \varphi_{mod})$ and scattering amplitude $\gamma(f_{exc}, P_{exc}, \varphi_{mod})$ to consequently obtain the partial derivatives with respect to flux as can be seen in Fig. 5. For the next process, we stored the maximum gains $G_\theta^{opt}(f_{exc}, P_{exc})$ and $G_\gamma^{opt}(f_{exc}, P_{exc})$ along with the corresponding fluxes φ_{mod}^{opt} and resonance circle parameters (i.e., radius r and center x_c). Resonance circle parameters determine the rotating frame required to calculate the resonator's phase using Eq. (13) when a detector signal is present. This calibration procedure allows us to get all the parameters required to obtain a demodulated signal time-trace.

1. Optimum readout parameters for open-loop

In order to find the optimum readout parameters, for each frequency f_{exc} and power P_{exc}, a small detector signal $\varphi_{det}[m]$ was added to the fluxes corresponding to the maximum gains φ_{mod}^{opt}. The transmission parameter calculated and the readout noise sources are included. Consequently, depending on the selected domain, resonator's phase $\theta[m]$ and scattering amplitude $\gamma[m]$ time-traces calculated and $\varphi_\theta[m]$ and $\varphi_\gamma[m]$ derived dividing them by their correspondent optimum open-loop gain coefficients. By means of Welch's method,[45] the white flux noise spectral density $\sqrt{S_{\Phi,white}}$ was calculated. The results of these simulations for both domains are shown in Fig. 7 for the case of $T_n = 4$ K, typical noise equivalent temperature of a cryogenic HEMT amplifier.[31] Red and green dashed lines in Fig. 7 represent maximum and minimum resonance frequencies according to Eq. (3), while dashed–dotted blue, black, and cyan represent the minimum noise (P_{exc}, f_{exc}) trajectories. These three trajectories describe the position followed by the optimum open-loop gains previously presented in Fig. 5. Colored stars are the local noise minimums at $P_{exc} = -70$ dBm, exactly at the same positions where the maximum gains were calculated in Fig. 5. As we previously mentioned, only additive noise was considered. Therefore, the optimum readout parameters are valid for this condition.

As can be seen in Fig. 7, the noise minimums for low powers always lie within the maximum and minimum resonant frequencies, and the optimum conditions for the scattering amplitude are symmetrically located on both sides of the optimum condition for the resonator's phase. In order to compare the demodulated noise values for both demodulation domains, the minimum noise levels corresponding to these trajectories were simulated again for two different additive noise temperatures. In line with new amplification technologies, we performed simulations in the Standard
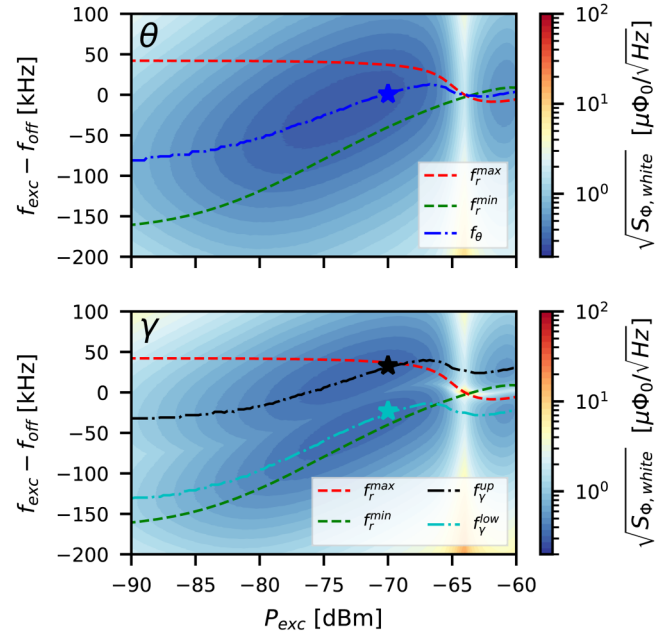
FIG. 7. Open-loop demodulated white noise flux density $\sqrt{S_{\Phi,white}}$ for both demodulation domains as a function of probe tone frequency f_{exc} and power P_{exc} for an additive noise temperature of $T_n = 4$ K. Red and green dashed lines represent maximum f_r^{max} and minimum f_r^{min} resonance frequencies respectively. (top) Resonator's phase demodulation—the dashed–dotted blue f_θ line is the optimum trajectory to achieve minimum noise. (bottom) Scattering amplitude demodulation—dashed–dotted black and cyan curves are the optimum trajectories to achieve both upper f_γ^{up} and lower f_γ^{low} local minimum noise values.

Quantum Limit[20,46] (SQL) condition with $T_n = hf_{exc}/k_B$ along with the $T_n = 4$ K previously used. The results are plotted together in Fig. 8. For these cases, flux noise levels can be estimated using the additive noise version of Eqs. (17) and (18),

$$\sqrt{S_\Phi^\theta} \approx \frac{1}{r}\sqrt{\frac{k_B T_n}{P_{exc}}}\left|\frac{\partial\theta}{\partial\Phi}\right|^{-1}, \qquad (25)$$

$$\sqrt{S_\Phi^\gamma} \approx \sqrt{\frac{k_B T_n}{P_{exc}}}\left|\frac{\partial\gamma}{\partial\Phi}\right|^{-1}, \qquad (26)$$

In accordance with these equations, at low power, the transfer coefficients remain constant and the noise level decreases proportionally to $\sqrt{S_{\Phi,white}} \propto 1/\sqrt{P_{exc}}$ until it reaches a plateau in which both open-loop gain values reach a level of around $P_{exc} \approx -63$ dBm where the μMUX becomes insensitive to flux variations. Using $P_{exc} = -70$ dBm, simulated optimum gain values yielded $G_\theta^{opt} = 4.90$ rad/Φ_0 and $G_\gamma^{opt,up} = G_\gamma^{opt,low} = 2.21/\Phi_0$ (see Fig. 5). Thus, for a resonance circle radius $r \approx Q_l/2Q_c \approx 0.49$, the calculated noise values results are $\sqrt{S_{\Phi,SQL}^\theta} \approx 0.071\mu\Phi_0/\sqrt{Hz}$ and
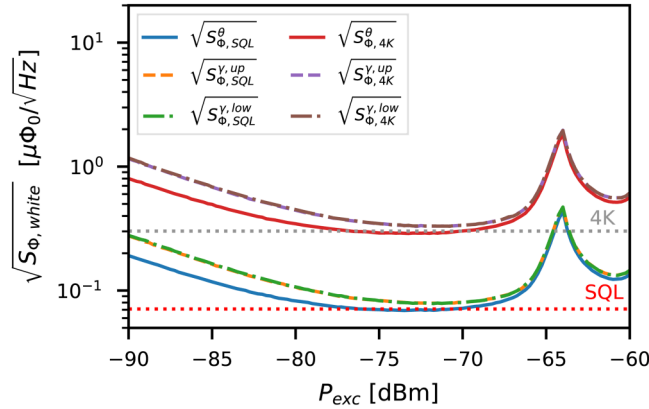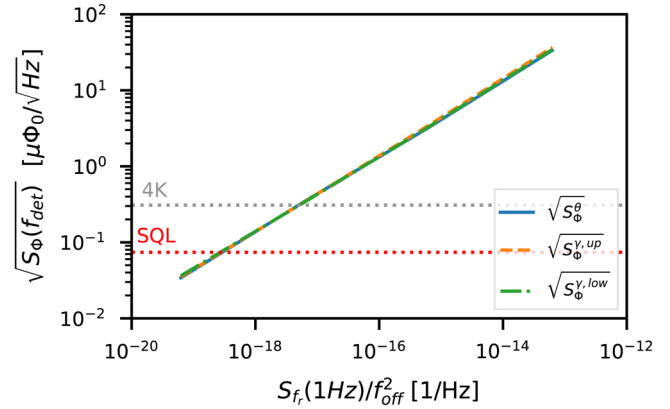
FIG. 8. Open-loop demodulated minimum white noise flux density $\sqrt{S_{\Phi,white}}$ for every demodulation domain as a function of power P_{exc} for both SQL and $T_n = 4$ K cases. Solid lines correspond to minimum noise for resonator's phase readout, while dashed and dashed–dotted lines are upper and lower local minimums for a scattering amplitude readout. Dotted gray and red lines are the minimum noise values for resonator's phase demodulation in the Standard Quantum Limit (SQL) and $T_n = 4$ K conditions evaluated at $P_{exc} = -70$ dBm.

FIG. 9. Open-loop demodulated white noise flux density $\sqrt{S_{\Phi,white}}$ as a function of the Two-Level System (TLS) noise level of $S_{f_r}(1\,\text{Hz})/f_{off}^2$ for both demodulation domains in the minimum additive noise condition for a constant $P_{exc} = -70$ dBm. As a reference, dotted red and gray lines represent the minimum noise values for resonator's phase demodulation in the case of the Standard Quantum Limit (SQL) and $T_n = 4$ K, respectively.

$\sqrt{S_{\Phi,SQL}^\gamma} \approx 0.08\mu\Phi_0/\sqrt{\text{Hz}}$ for the SQL, in contrast to $\sqrt{S_{\Phi,4K}^\theta}$ $\approx 0.30\mu\Phi_0/\sqrt{\text{Hz}}$ and $\sqrt{S_{\Phi,4K}^\gamma} \approx 0.34\mu\Phi_0/\sqrt{\text{Hz}}$ with $T_n = 4$ K, in well agreement with the simulations. Dotted red and gray lines represent the aforementioned noise values in the case of resonator's phase readout. Leaving aside technical difficulties that may be encountered when implementing the demodulation of one of the domains, which will be discussed in Subsections IV A 2 and IV A 3, there is no strong argument based on noise performance to decide for either domain. This is given by the non-appreciable noise differences in the simulation results. Therefore, we will evaluate the impact of the remaining noise sources in order to find considerable differences that would indicate the existence of a preferential domain.

2. TLS and multiplicative noise impact for open-loop

In order to quantify the impact of the non-additive noise sources, we performed individual simulations for each noise source under the optimum readout parameters for additive noise, represented with stars in Fig. 7. As mentioned earlier, two-level system noise is one of the most common noise sources and particularly important in an open-loop readout due to its frequency dependence.[36] Here, TLS noise was represented by its fractional frequency density S_{f_r}/f_{off}^2 with a frequency slope of $1/f$ and taking values from 6.25×10^{-20} Hz^{-1} to 6.25×10^{-14} Hz^{-1} when evaluated at 1 Hz. Due to the TLS noise saturation depending on the readout power,[36] it is worth mentioning that TLS noise is specified for $P_{ext} = -70$ dBm. Simulation results for each domain measured at detector frequencies of $f_{det} \approx 762$ Hz are shown in Fig. 9. As in the previous plots, the minimum noise values for the SQL and $T_n = 4$ K were included as a reference.

Results in Fig. 9 allow us to set maximum TLS noise levels of $S_{f_r}(1\,\text{Hz})/f_{off}^2 = 3 \times 10^{-18}$ Hz^{-1} and $S_{f_r}(1\,\text{Hz})/f_{off}^2 = 6.6$ $\times 10^{-17}$ Hz^{-1} for the SQL and $T_n = 4$ K, respectively, avoiding the TLS as a dominant noise source, but once again, showing no preferential demodulation domain.

Contrary to the TLS noise, multiplicative and additive noise sources can be compared directly in the same NSD units. Therefore, the simulations were performed as a function of the NSD values for each noise source in the same conditions as before using $P_{exc} = -70$ dBm. Equivalent noise temperatures starting from the SQL with $T_n = hf_{exc}/k_B \approx 0.24$ K, to $T_n = 8$ K, corresponding to NSDs from -135 to -120 dBc/Hz were used in the case of additive noise. While for phase and amplitude readout noise, NSD going from -130 to -100 dBc/Hz. Since both local minimums for a scattering amplitude yield the same demodulated noise for open-loop demodulation, only the upper local minimum is considered in the following analysis. The results of these simulations as a function of the NSD are shown in Fig. 10. As demonstrated previously, a resonator's phase readout leads to slightly lower noise than a scattering amplitude readout for the same NSD. In addition, as expected from Table II, noise levels scale proportional to NSD with $\sqrt{S_\Phi} \propto \sqrt{NSD}$, being additive noise the dominant noise source compared with multiplicative sources for equal NSD values. When considering non-correlated noise sources acting together, the total system noise is the quadrature summation of all individual contributions. Therefore, we defined a rejection factor A for each noise source and a demodulation domain equal to the NSD difference with respect to the additive NSD that would result in the same demodulated noise level. This factor is represented with a black arrow in Fig. 10 for the case of scattering amplitude demodulation and is equal to the distance in NSD units between parallel dashed lines for a constant flux noise density. Thus, for scattering amplitude demodulation, there is a ≈ 10 dB rejection of
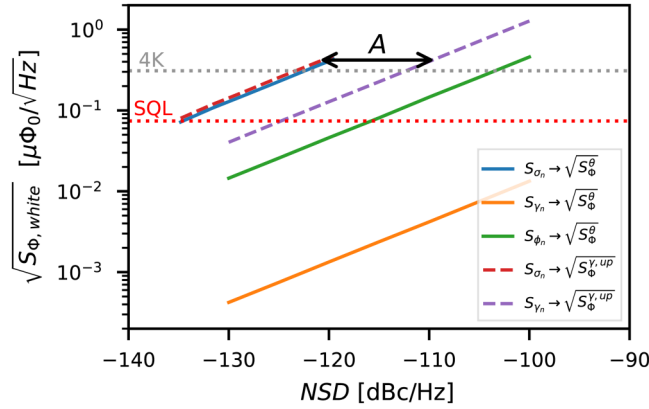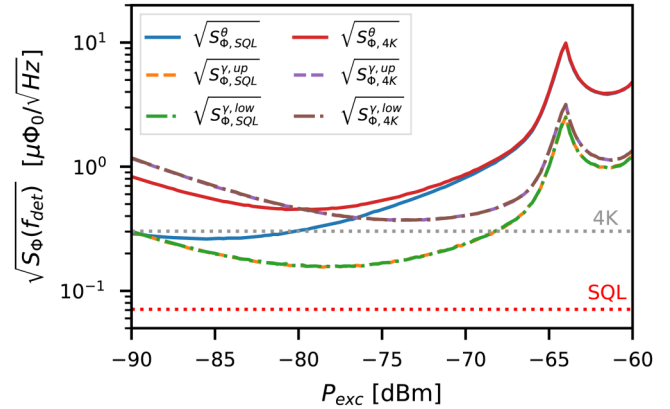
FIG. 10. Open-loop demodulated white flux noise density $\sqrt{S_{\Phi,white}}$ for every demodulation domain as a function of the noise spectral densities (NSDs) for each noise source in the minimum additive noise condition for a constant $P_{exc} = -70$ dBm. Dashed lines correspond to a scattering amplitude domain, while solid lines are for a resonator's phase readout. Gray and red dotted lines are plotted as a reference and are equal to the white noise values for the Standard Quantum Limit (SQL) and for $T_n = 4$ K for a resonator's phase readout. As an example, the black arrow represents the amplitude noise rejection factor A in a scattering amplitude domain readout.

FIG. 11. Open-loop demodulated flux noise density $\sqrt{S_{\Phi}(f_{det})}$ for every demodulation domain as a function of power P_{exc} for both SQL and $T_n = 4$ K cases. Solid lines correspond to minimum noise for a resonator's phase readout, while dashed and dashed–dotted lines are upper and lower local minimums for a scattering amplitude readout. Dotted gray and red lines are the minimum noise values for resonator's phase demodulation in the Standard Quantum Limit (SQL) and $T_n = 4$ K conditions evaluated at $P_{exc} = -70$ dBm.

amplitude noise. In contrast, using resonator's phase demodulation, there are ≈ 19 dB and more than 40 dB rejection values for phase and amplitude noise, respectively. Particularly, scattering amplitude demodulation is more sensitive than resonator's phase demodulation to amplitude noise because the readout tone is positioned further away from the resonance where its projection is considerably greater compared to phase noise and the scattering amplitude open-loop gain lower. On the contrary, resonator's phase demodulation is more sensitive to phase noise because the maximum open-loop gain requires the probing tone in resonance where phase noise projection is maximum (see Fig. 2).

3. Optimum domain for open-loop

Previous results suggest that maximum sensitivity is achieved in the resonator's phase domain due to the lower demodulated noise level in the additive noise case and high rejection to multiplicative noise sources compared to a scattering amplitude domain. Unfortunately, this is not a realistic scenario in the case of an open-loop readout. Phase and amplitude noise spectral components [Eq. (11)] usually grow rapidly for small frequency offsets far exceeding additive noise, impacting directly in the detector signal. As an example, in order to determine the expected open-loop performance of a real SDR readout system,[38] the measured noise values shown in Fig. 4 were included in our simulation framework. Since the TLS noise did not show a preferential readout region and we assume a proper resonator design, it was not included in this case. The results of the demodulated noise for every domain for both SQL and $T_n = 4$ K additive noise conditions are shown in Fig. 11.

Clearly, the demodulated noise is dominated by the multiplicative noise, and its effect is most noticeable at high powers and

near the SQL.[46] In the case of the resonator's phase domain, its noise is completely dominated by the multiplicative noise values of $S_{\phi}(f_{det}) \approx -96$ dBc/Hz and $S_{\gamma}(f_{det}) \approx -116$ dBc/Hz for phase and amplitude, respectively. Both are considerably larger than the additive noise at the detector frequency $S_{\sigma}(f_{det})$ (see colored stars in Fig. 4). Noise levels at $P_{exc} = -70$ dBm are $\sqrt{S_{\Phi}^{\theta}(f_{det})} \approx 0.82 \mu\Phi_0/\sqrt{Hz}$ and $\sqrt{S_{\Phi}^{\theta}(f_{det})} \approx 0.24 \mu\Phi_0/\sqrt{Hz}$ for the SQL, while $\sqrt{S_{\Phi}^{\theta}(f_{det})} \approx 0.87 \mu\Phi_0/\sqrt{Hz}$ and $\sqrt{S_{\Phi}^{\gamma}(f_{det})} \approx 0.40 \mu\Phi_0/\sqrt{Hz}$ for the $T_n = 4$ K case. All of them are consistent with the values shown in Fig. 10 for their respective NSD levels.

While phase noise can be reduced at lower frequencies using an ultra-low phase noise synthesizer as suggested in Appendix B and TLS can be strongly reduced properly choosing resonator materials and geometry,[36] they are still a problem especially in the case of bolometric applications. Therefore, the FRM technique mentioned above in Sec. III D 2 can be used to mitigate these effects along with other limitations previously mentioned.
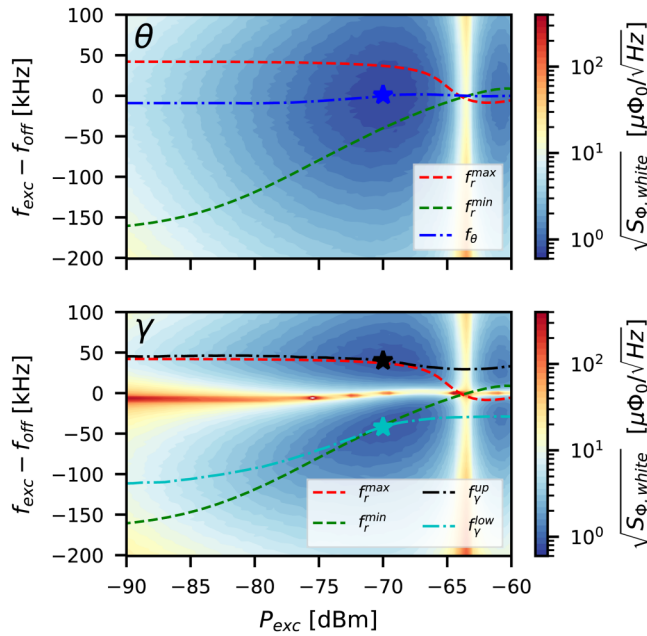
B. Flux-ramp demodulation noise performance

Similarly to the open-loop demodulation, we replicated the noise characterization procedure of a real μMUX device. For the determination of the noise density in the FRD scheme described by Eqs. (21) and (20), first, we generated the modulation flux $\varphi_{mod}[m]$ and the detector signal $\varphi_{det}[m]$ using the parameters described in Table III. Both fluxes were added; $f_r[m]$ and the transmission parameter $S_{21}(f_{exc}, P_{exc}, \varphi_{mod})[m]$ consequently iteratively calculated. Later, using the circle parameters previously stored, resonator's phase $\theta(f_{exc}, P_{exc}, \varphi)[m]$ and scattering amplitude $\gamma(f_{exc}, P_{exc}, \varphi_{mod})[m]$ time-traces were obtained. Finally, we apply the FRD for both domains in order to get the detector

30 September 2024 12:09:50

signal time-traces $\varphi_\theta[n]$ and $\varphi_\gamma[n]$. Here, we used n instead of m as a consequence of the decimation produced by the FRD[29,43] (see Fig. 6).

1. Optimum readout parameters for FRD

The demodulated detector time-traces $\varphi_{\text{det}}[n]$ for both domains were calculated as a function of the frequency f_{exc} and power P_{exc} considering only additive noise with $T_n = 4\,\text{K}$. By means of Welch's method,[45] the white flux noise spectral density $\sqrt{S_{\Phi,white}}$ was calculated. The results of these simulations for both domains are shown in Fig. 12. Red and green dashed lines represent maximum and minimum resonance frequencies, while dashed–dotted blue, black, and cyan the minimum noise $(P_{\text{exc}}, f_{\text{exc}})$ trajectories. Colored stars are the absolute noise minimums at $P_{\text{exc}} \approx -70\,\text{dBm}$ for both domains.

In principle, we would assume that the noise minima will also follow the trajectories previously found for the open-loop scenario (Fig. 7). However, this is not the case, and the trajectories mainly differ, only approaching each other at high powers. This behavior is mainly determined by the spectral components of the resonator's phase and scattering amplitude time-traces described by their
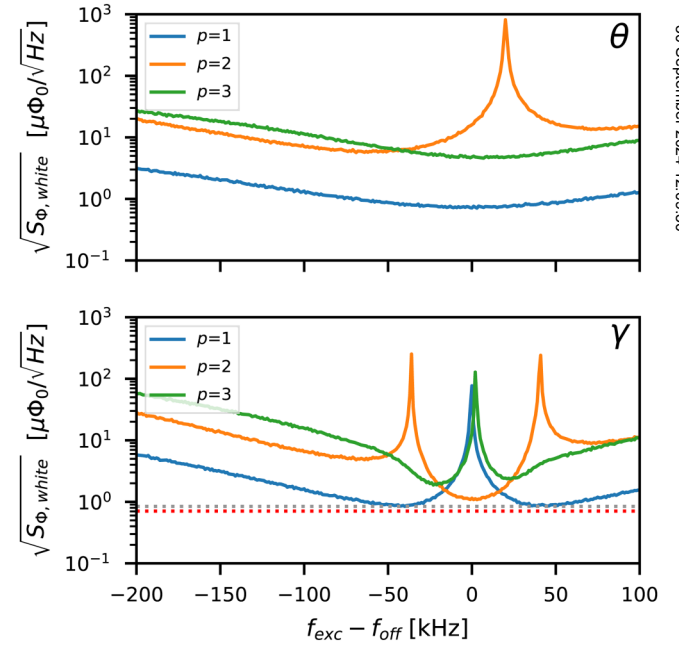
Fourier series as

$$\theta(t) \approx \Theta_0 + \sum_{p=1}^{\infty} \Theta_p \sin(2\pi p f_{\text{mod}}t + \lambda_p), \quad (27)$$

$$\gamma(t) \approx \Gamma_0 + \sum_{p=1}^{\infty} \Gamma_p \sin(2\pi p f_{\text{mod}}t + \varepsilon_p), \quad (28)$$

where the fundamental frequency is $f_{\text{mod}} = n_{\Phi_0}f_{\text{ramp}}$ (also called the SQUID frequency) and $\Theta_p, \Gamma_p, \lambda_p, \epsilon_p$ are amplitude and phase spectral coefficients. Based on the FRM,[29] we can assume that the detector signal changes the instantaneous frequency of each harmonic component $f_{\text{dem}} = p \cdot f_{\text{mod}}$ and consequently, each component is phase modulated. However, while the modulation index is given by the detector signal, the carrier power depends on the amplitude spectral components of each domain (i.e., Θ_p and Γ_p). Due to the fact that the first component is usually demodulated, noise values increase when either Θ_p or Γ_p decreases. In order to probe this, we swept f_{exc} at a constant power of $P_{\text{exc}} = -70\,\text{dBm}$, and the detector signal was demodulated for each harmonic component changing p in Eqs. (20) and (21). Only one period was discarded considering that the flux-ramp transient lasts less than one period of the highest modulating frequency harmonic. The results of the simulation are shown in Fig. 13.

FIG. 12. Flux-ramp demodulated white flux noise density $\sqrt{S_{\Phi,white}}$ for both demodulation domains as a function of probe tone frequency f_{exc} and power P_{exc}. (top) Resonator's phase demodulation—red and green dashed lines represent maximum f_r^{max} and minimum f_r^{min} resonance frequencies, respectively. Dashed–dotted blue lines f_θ show the optimum trajectory to achieve minimum noise. (bottom) Scattering amplitude demodulation—dashed–dotted black and cyan curves are the optimum trajectories to achieve both upper f_γ^{up} and lower f_γ^{low} local minimum noise values. Hamming windows function with $n_{\text{disc}} = 1$ and $n_{\Phi_0} = 4$ were used.

FIG. 13. Flux-ramp demodulated white flux noise density $\sqrt{S_{\Phi,white}}$ as a function of f_{exc} for every demodulated domain and selected FRM component $f_{\text{dem}} = p \cdot f_{\text{mod}}$ for constant $P_{\text{exc}} = -70\,\text{dBm}$ and additive noise temperature of $T_n = 4\,\text{K}$. (top) Resonator's phase demodulation. (bottom) Scattering amplitude demodulation. Red and gray lines show resonator's phase and scattering amplitude noise minimums, respectively. Hamming window functions with $n_{\text{disc}} = 1$ and $n_{\Phi_0} = 4$ were used.

Blue traces in both panels of Fig. 13 correspond to the demodulation of the first harmonic component $p = 1$, consistent with the results of Fig. 12. Dotted red and gray lines are the minimum demodulated white flux noise for resonator's phase and scattering amplitude, respectively, achieved at conditions represented by the blue, black, and cyan stars. Like in the open-loop scheme, the resonator's phase domain gives the lowest possible noise, although the difference with scattering amplitude demodulation is not considerable. In the case of the resonator's phase, we can see that demodulated noise for the first component is always lower than the rest. On the contrary, in the case of a scattering amplitude readout, when the probe tone f_{exc} is close to the unaltered resonance frequency f_{off}, noise diverges for the first and third demodulated component, while for the second, there is a minimum in accordance with the results presented by Schuster.[22] Therefore, the absolute minimum noise conditions imply the demodulation of the first harmonic at its maximum amplitude (i.e., Θ_1^{max} and Γ_1^{max}). Since the total power is spread out between harmonics, this is fulfilled when the sum of the powers of the other harmonics reach their minimums. On the other hand, for a fixed f_{exc}, the spectral components are determined by P_{exc}.[26] When power increases P_{exc}, both β_{eff} and η decrease, leading again to a sinusoidal response in the resonator's phase and the scattering amplitude until there is no response (i.e., $\Theta_p \approx \Gamma_p \approx 0$). Taking advantage of the fact that the resonator's phase and the scattering amplitude behave as sinusoidal signals at high powers, Eqs. (22) and (23) in the additive noise case can be easily calculated considering $\theta(\Phi) \approx \Theta_1 \sin(2\pi\Phi/\Phi_0)$ $\gamma(\Phi) \approx \Gamma_1 \sin(2\pi\Phi/\Phi_0)$ yielding to[20]

$$\sqrt{S_\Phi^\theta} \approx \frac{1}{r} \frac{\sqrt{2\kappa/\alpha}}{2\pi\Theta_1} \sqrt{\frac{k_B T_n}{P_{exc}}}, \tag{29}$$

$$\sqrt{S_\Phi^\gamma} \approx \frac{\sqrt{2\kappa/\alpha}}{2\pi\Gamma_1} \sqrt{\frac{k_B T_n}{P_{exc}}}. \tag{30}$$

To verify the validity of these expressions, to later use them to estimate system temperature T_{sys}, first, we numerically determined the amplitude of the fundamental resonator's phase and scattering amplitude components yielding $\Theta_1 \approx 0.63$ rad and $\Gamma_1^{up} \approx \Gamma_1^{low} \approx 0.27$. Second, we demodulated white flux noise for both domains as a function of probe tone frequency f_{exc} at constant power $P_{exc} \approx -70$ dBm for three different cases: (1) boxcar window $w[n]$ without discarding, (2) boxcar window and one period discarded, and (3) the Hamming window with one period discarded. As we mentioned earlier in Sec. III D 2, discarding one period is sufficient to avoid the transient present at the beginning of each period of the sawtooth-shaped flux signal. For all cases, we used $n_{\Phi_0} = 4$ and the parameters in Table III. The results presented in Fig. 14 for the non-discarding case were $\sqrt{S_\Phi^\theta} \approx 0.52\mu\Phi_0/\sqrt{Hz}$ and $\sqrt{S_\Phi^\gamma} \approx 0.62\mu\Phi_0/\sqrt{Hz}$ for the phase and amplitude, respectively, while in the second case, $\sqrt{S_\Phi^\theta} \approx 0.61\mu\Phi_0/\sqrt{Hz}$ and $\sqrt{S_\Phi^\gamma} \approx 0.72\mu\Phi_0/\sqrt{Hz}$. Last, using the Hamming window, $\sqrt{S_\Phi^\theta} \approx 0.71\mu\Phi_0/\sqrt{Hz}$ and $\sqrt{S_\Phi^\gamma} \approx 0.84\mu\Phi_0/\sqrt{Hz}$. These values are in well agreement with expressions (29) and (30) using the
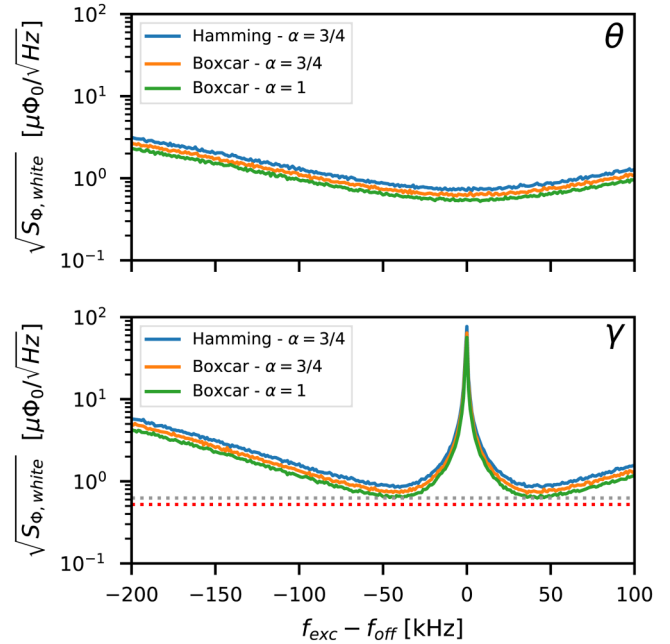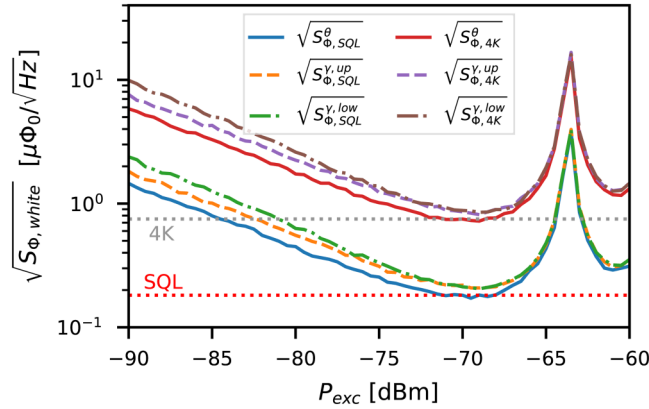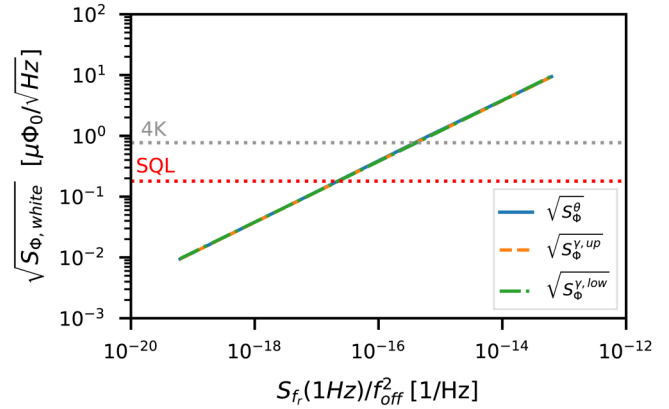

FIG. 14. Flux-ramp demodulated white flux noise density $\sqrt{S_{\Phi,white}}$ as a function of f_{exc} for different window functions $w(t)$ and the number of discarded periods n_{disc} with constant $P_{exc} = -70$ dBm and an additive noise temperature of $T_n = 4$ K. (top) The resonator's phase and (bottom) the scattering amplitude. Red and gray lines show phase and amplitude noise minimums, respectively, for a Boxcar window function, without periods discarded.

aforementioned Θ_1 and Γ_1 values. As expected, discarding a period yielded a degradation of $\sqrt{4/3} \approx 1.15$, while the Hamming window $\sqrt{4\kappa/3} \approx 1.35$. This corresponds to a factor $\kappa = 1.37$ coincident with the equivalent noise bandwidth of the Hamming window with respect to the Boxcar. Although the Hamming window improves linearity,[43] its main-lobe is wider compared to the boxcar window, leading to an increase in the noise level. For the purpose of this work, this degradation is not important since it affects both domains equally.

Similar to the open-loop demodulation, the noise in the optimal trajectories for both domains was determined for the SQL and $T_n = 4$ K. The results are shown in Fig. 15. Again, the resonator's phase readout provides the best performance, and noise densities decrease with $\sqrt{S_{\Phi,white}} \propto 1/\sqrt{P_{exc}}$ for both domains reaching minimums at $P_{exc} = -70$ dBm. Unlike the open-loop case, both amplitude minima differ at low powers, while at high powers, they coincide due to the sinusoidal behavior explained earlier. In agreement with Eqs. (29) and (30), noise values in the SQL are $\sqrt{S_{\Phi,SQL}^\theta} \approx 0.18\mu\Phi_0/\sqrt{Hz}$ and $\sqrt{S_{\Phi,SQL}^\gamma} \approx 0.22\mu\Phi_0/\sqrt{Hz}$ being $\sqrt{T_{4K}/T_{SLQ}} \approx 4$ lower than the $T_n = 4$ K case. As expected, these values represent a degradation of $c_{deg}^\theta \approx 2.53$ and $c_{deg}^\gamma \approx 2.8$ with respect to open-loop demodulation. Smaller values can be achieved removing the windows or not discarding periods depending on the

FIG. 15. Flux-ramp demodulated minimum white flux noise density $\sqrt{S_{\Phi,white}}$ for every demodulation domain as a function of power P_{exc} and additive noise temperature of $T_n = 4\,\text{K}$. Solid lines correspond to minimum noise for a resonator's phase readout, while dashed and dashed–dotted lines are upper and lower local minimums for a scattering amplitude readout. As a reference, dotted red and gray lines represent the minimum noise values for resonator's phase demodulation with a power of $P_{exc} = -70\,\text{dBm}$ in the case of the Standard Quantum Limit (SQL) and $T_n = 4\,\text{K}$, respectively. Hamming window functions with $n_{disc} = 1$ and $n_{\Phi_0} = 4$ were used.

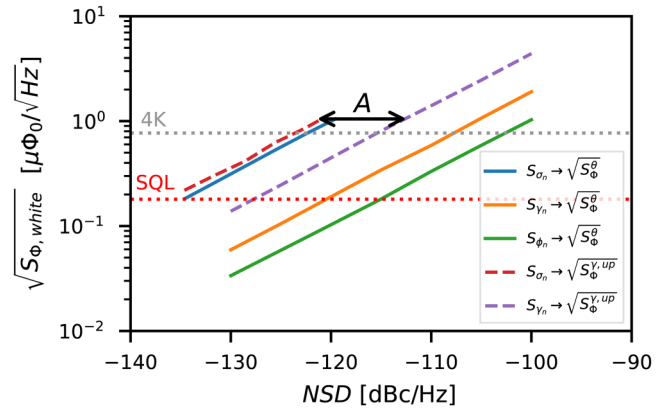FIG. 16. Flux-ramp demodulated white flux noise density $\sqrt{S_{\Phi,white}}$ as a function of the Two-Level System (TLS) noise level of S_{f_r}/f_{off} for both demodulation domains in the minimum additive noise condition for a constant $P_{exc} = -70\,\text{dBm}$. As a reference, dotted red and gray lines represent the minimum noise values for resonator's phase demodulation with a power of $P_{exc} = -70\,\text{dBm}$ in the case of the Standard Quantum Limit (SQL) and $T_n = 4\,\text{K}$, respectively. Hamming window function with $n_{disc} = 1$ and $n_{\Phi_0} = 4$ were used ($\alpha = 4/3$).

linearity requirements or the flux-ramp transient duration. Despite the imposed degradation, FRM provides other advantages as we will demonstrate below using our simulation framework in Secs. IV B 2 and IV B 3.

2. TLS and multiplicative noise impact for FRD

As shown in Sec. IV A 2, we performed simulations to evaluate the impact of both TLS noise and multiplicative readout system noise for FRD. Starting with TLS, we determined the demodulated noise $\sqrt{S_{\Phi,white}}$ at the detector frequencies f_{det} for the same fractional frequency densities $S_{f_r}(1\,\text{Hz})/f_{off}^2$ values used before. The results are shown in Fig. 16 for both domains at the optimum conditions represented by stars in Fig. 12. It can be seen that although the noise level increased with respect to the un-modulated case, for the same noise density, TLS noise represents a lower impact with respect to additive noise levels represented by the red and gray dotted lines. This is due to the demodulation process that down-converts the information signal from the carrier frequency $f_{mod} \approx 61\,\text{kHz}$, and therefore, the noise is evaluated at the same frequency $S_{f_r}(f_{mod})/f_{off}^2$. This value is considerably lower than the value at $S_{f_r}(f_{det})/f_{off}^2$ due to the $1/f$ TLS dependency. Therefore, relaxing the maximum TLS noise requirements to $S_{f_r}(1\,\text{Hz})/f_{off}^2 = 2 \times 10^{-17}\,\text{Hz}^{-1}$ and $S_{f_r}(1\,\text{Hz})/f_{off}^2 = 4 \times 10^{-16}\,\text{Hz}^{-1}$ for the SQL and $T_n = 4\,\text{K}$, respectively. As far as the readout domain is concerned, results show again no preference for the resonator's phase or scattering amplitude demodulation at higher powers, leaving multiplicative noise as the main factor to decide if there is an optimal readout domain.

Demodulated noise results for multiplicative sources under the optimum readout condition for additive noise found in Sec. IV B 1 as a function of NSD are shown in Fig. 17. As seen in previous results, the resonator's phase domain is the optimal domain for the additive noise case, while the other noise sources remain negligible for the same NSD values. All noise demodulated

FIG. 17. Flux-ramp demodulated white flux noise density for every demodulation domain and power for additive noise with 4 K. As a reference, dotted red and gray lines represent the minimum noise values for resonator's phase demodulation with a power of $P_{exc} = -70\,\text{dBm}$ in the case of the Standard Quantum Limit (SQL) and $T_n = 4\,\text{K}$, respectively. Hamming window functions with $n_{disc} = 1$ and $n_{\Phi_0} = 4$ were used. As an example, the black arrow represents the amplitude noise rejection factor A in a scattering amplitude domain readout.

30 September 2024 12:09:50

values increase with respect to the open-loop case, following the same dependence with $\sqrt{S_\Phi} \propto \sqrt{NSD}$. However, all previously defined rejection factors decreased from 10 to 8 dB for amplitude noise in the scattering amplitude domain, while for the resonator's phase demodulation from 19 to 18 dB and from 40 to 14 dB for phase and amplitude noise, respectively. As expected, all rejection factors decreased as a consequence of the FRM. Particularly, phase demodulation became more sensitive to amplitude noise when the readout tone is positioned further away from the resonance, where its projection is considerably greater and the gain is lower. On the contrary, phase noise in these positions is lower; therefore, it has less impact. However, as we demonstrated before, system noise depends on the characteristics of the readout hardware used.

3. Optimum domain for FRD

Similar to the open-loop demodulation case, we used the simulation framework in order to predict the system noise performance of the SDR system used as an example. Measured noise values shown in Fig. 4 using magenta and cyan triangles were included in our simulation framework and again, TLS noise was not considered. The results of the flux-ramp demodulated noise for every domain and both SQL and $T_n = 4\,K$ additive noise conditions are shown in Fig. 18. Once again, the scattering amplitude readout shows the best performance when a real SDR readout system is used, and the impact of multiplicative noise became more relevant for the SQL scenario. In the case of the resonator's phase domain, it is completely dominated by the phase noise of the readout system, which has a value of $S_\phi(f_{mod}) \approx -108\,dBc/Hz$ at the frequency f_{mod}. Amplitude noise at the same frequency with $S_\gamma(f_{mod}) \approx -130\,dBc/Hz$ does not have NSD to represent considerable degradation for any of both scenarios. Clearly, like TLS, FRM helped in reducing the low-frequency multiplicative noise
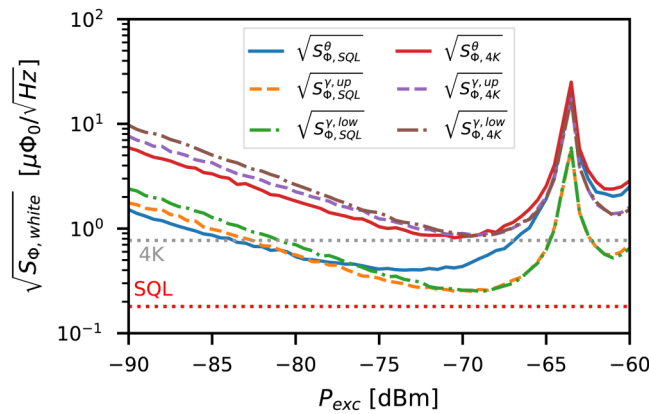
FIG. 18. Flux-ramp demodulated white flux noise density $\sqrt{S_{\Phi,white}}$ for every demodulation domain as a function of power P_{exc} and additive noise temperature of $T_n = 4\,K$. As a reference, dotted red and gray lines represent the minimum noise values for resonator's phase demodulation with a power of $P_{exc} = -70\,dBm$ in the case of the Standard Quantum Limit (SQL) and $T_n = 4\,K$, respectively. Hamming window functions with $n_{disc} = 1$ and $n_{\Phi_0} = 4$ were used.

compared to the open-loop scheme. Quantitatively, noise levels at $P_{exc} = -70\,dBm$ are $\sqrt{S_\Phi^\theta} \approx 0.43\mu\Phi_0/\sqrt{Hz}$ and $\sqrt{S_\Phi^\gamma} \approx 0.24\mu\Phi_0/\sqrt{Hz}$ for the SQL and $\sqrt{S_\Phi^\theta} \approx 0.84\mu\Phi_0/\sqrt{Hz}$ and $\sqrt{S_\Phi^\gamma} \approx 0.90\mu\Phi_0/\sqrt{Hz}$ for the $T_n = 4\,K$ case, all of them consistent with the values shown in Fig. 17 for their respective NSD levels.

V. DISCUSSION

As a summary, Table IV condenses all demodulated noise values for both demodulation schemes and readout domains. Here, $\sqrt{S_\Phi^{T_n}}$ represents the demodulated noise levels considering only the additive noise contribution T_n, while $\sqrt{S_\Phi^{T_{sys}}}$ takes into account the contributions of multiplicative and additive noise acting simultaneously. Based on these results and using Eqs. (25), (26), (29), and (30), it is possible to calculate an equivalent system temperature $\sqrt{S_\Phi^{T_{sys}}}$, which reflects the measured noise. This would be the noise temperature that one would infer from the flux noise measurements and attribute it directly to the additive noise, not knowing that it is also produced by the multiplicative noise.

Table IV shows a large difference between T_n and T_{sys} for the open-loop demodulation of the resonator's phase in contrast to the scattering amplitude. This is a result of the excessive phase noise level measured at detector frequencies $S_\phi(f_{det})$ compared to the additive $S_\sigma(f_{det})$ and amplitude noise $S_\gamma(f_{det})$ as can be seen in Fig. 4. For the case of FRD, the difference between T_n and T_{sys} is lower due to the fact that additive and multiplicative spectral densities are evaluated at modulation frequencies f_{mod} [i.e., $S_\sigma(f_{mod}), S_\phi(f_{mod}), S_\gamma(f_{mod})$] where there is no significant difference between noise levels. Therefore, the system noise temperature tends to the additive noise temperature $T_{sys} \to T_n$. We can conclude that for this particular SDR system, the optimal readout domain is the scattering amplitude γ and that the FRD allows one to avoid the multiplicative noise at low frequencies representing a reduction in

TABLE IV. Comparative between demodulated flux noise density $\sqrt{S_\Phi^{T_n}}$ considering only the additive noise contribution described with T_n and the demodulated flux noise density $\sqrt{S_\Phi^{T_{sys}}}$ considering all noise sources acting together as an equivalent additive system noise temperature T_{sys}. The results are presented for both readout schemes and demodulation domains. In the Standard Quantum Limit (SQL), the additive noise temperature corresponds to $T_n \approx 0.24\,K$ at $f_{exc} = 5\,GHz$. Here, OPL stands for an open-loop.

Scheme	Domain	T_n	$\sqrt{S_\Phi^{T_n}}$	T_{sys}	$\sqrt{S_\Phi^{T_{sys}}}$
OPL	θ	≈ 0.24	$0.071\mu\Phi_0/\sqrt{Hz}$	29	$0.82\mu\Phi_0/\sqrt{Hz}$
OPL	θ	4	$0.30\mu\Phi_0/\sqrt{Hz}$	33	$0.87\mu\Phi_0/\sqrt{Hz}$
OPL	γ	≈ 0.24	$0.08\mu\Phi_0/\sqrt{Hz}$	2	$0.24\mu\Phi_0/\sqrt{Hz}$
OPL	γ	4	$0.34\mu\Phi_0/\sqrt{Hz}$	5.6	$0.40\mu\Phi_0/\sqrt{Hz}$
FRD	θ	≈ 0.24	$0.18\mu\Phi_0/\sqrt{Hz}$	1.4	$0.43\mu\Phi_0/\sqrt{Hz}$
FRD	θ	4	$0.71\mu\Phi_0/\sqrt{Hz}$	5.1	$0.84\mu\Phi_0/\sqrt{Hz}$
FRD	γ	≈ 0.24	$0.22\mu\Phi_0/\sqrt{Hz}$	0.4	$0.24\mu\Phi_0/\sqrt{Hz}$
FRD	γ	4	$0.84\mu\Phi_0/\sqrt{Hz}$	4.5	$0.90\mu\Phi_0/\sqrt{Hz}$

the demodulated flux noise. Although the multiplicative noise can be mitigated, it still represents degradation in sensitivity particularly when working in conditions close to the SQL.

Simulations presented in this article contributed to improve system noise estimations finding the maximum noise values that can be managed for a given sensitivity. Thus, it enables the optimization of the associated μMUX, cold, and warm-temperature readout systems. Although for this work, the criterion for the selection of optimal parameters was found to be based on the condition of minimum readout noise, two important factors must be taken into account. First, for a large number of channels N, the total power at the output of the μMUX grows with $P_{out} \propto N$ and can saturate the HEMT amplifier degrading the noise performance.[31] Particularly, in the case presented in Sec. IV B 1, there is no substantial difference, the resonator's phase demodulation presented $P_{out} \approx -82\,\text{dBm}$ with respect to the scattering amplitude with $P_{out} \approx -79\,\text{dBm}$ for a $P_{exc} = -70\,\text{dBm}$. Second, while the phase demodulation yielded better results for the additive noise case, the scattering amplitude is robust to other types of noise, as well as not requiring a resonance circle transformation, which can be affected by phase variations[30] of the RF components and requires more digital resources to be implemented.[40,42]

As mentioned at the beginning of this article, the presented analysis applies only to the readout by a single fixed tone. A recently proposed method called tone-tracking tries to overcome the aforementioned limitation imposed by the saturation of the HEMT amplifier when reading a large number of detectors. This system uses a feedback system that corrects the frequency of the probing tone to keep it in resonance and, consequently, minimizing the peak power at the μMUX output.[15,21] Given the advantages of this system, future work will consider extending the results of this work to the analysis of this innovative readout technique.

VI. CONCLUSION

We successfully extended the capabilities of previously developed simulation frameworks for an μMUX readout, including multiplicative noise sources, as well as the ability of demodulating data in different domains. Through different simulations, the optimum readout parameters to achieve the lowest possible readout noise for a μMUX device optimized for bolometric applications were found in both open-loop and flux-ramp demodulation schemes. We probe that the optimal readout parameters in the case of open-loop and flux-ramp demodulation are different and are mainly determined by the first harmonic component used for demodulation. We demonstrate that the dominant noise source in both cases is the additive noise and the optimal demodulation domain for this condition is the resonator's phase. Under the minimum noise parameters for additive noise, the impact of the multiplicative sources was assessed. An example using a typical SDR readout system was presented and the impact on the system noise was estimated. Due to the higher readout phase noise, the results showed considerable degradation of the system noise when demodulation is performed in the resonator's phase domain. Contrarily, demodulation in the scattering amplitude domain yielded the minimum noise dominated by additive noise. As expected, degradation becomes more evident close to the SQL when parametric amplifiers

are used. Additionally and as an integral part of this work, the performance of the flux-ramp demodulation using different windows, the effect of discarding periods, as well as the demodulation of different harmonic components were evaluated and contrasted with the open-loop case. Last but not least, it is important to note that the noise analysis of the readout system presented here is not only useful for the design of an SDR readout for μMUX systems, but also for different frequency domain multiplexed superconducting devices, such as MKIDs and QUBITs.

AUTHOR DECLARATIONS

Conflict of Interest

The authors have no conflicts to disclose.

Author Contributions

M. E. García Redondo: Conceptualization (lead); Data curation (lead); Formal analysis (lead); Investigation (lead); Methodology (lead); Software (lead); Validation (lead); Visualization (lead); Writing – original draft (lead); Writing – review & editing (lead). **N. A. Müller:** Conceptualization (equal); Data curation (equal); Formal analysis (equal); Investigation (equal); Methodology (equal); Software (supporting); Validation (equal); Visualization (supporting); Writing – original draft (supporting); Writing – review & editing (equal). **J. M. Salum:** Conceptualization (equal); Data curation (equal); Formal analysis (equal); Investigation (equal); Methodology (supporting); Software (supporting); Validation (supporting); Visualization (supporting); Writing – original draft (supporting); Writing – review & editing (equal). **L. P. Ferreyro:** Conceptualization (equal); Data curation (equal); Formal analysis (equal); Investigation (equal); Methodology (supporting); Software (supporting); Validation (supporting); Visualization (supporting); Writing – original draft (supporting); Writing – review & editing (equal). **J. D. Bonilla-Neira:** Conceptualization (supporting); Data curation (supporting); Formal analysis (supporting)); Investigation (supporting); Methodology (supporting); Writing – review & editing (equal). **J. M. Geria:** Conceptualization (supporting); Data curation (supporting); Formal analysis (supporting); Investigation (supporting); Methodology (supporting); Writing – review & editing (equal). **J. J. Bonaparte:** Funding acquisition (supporting); Investigation (supporting); Methodology (supporting); Resources (supporting); Writing – review & editing (equal). **T. Muscheid:** Conceptualization (supporting); Formal analysis (supporting); Software (supporting); Writing – review & editing (equal). **R. Gartmann:** Conceptualization (supporting); Formal analysis (supporting); Software (supporting); Writing – review & editing (equal). **A. Almela:** Conceptualization (equal); Data curation (equal); Formal analysis (equal); Funding acquisition (equal);

DATA AVAILABILITY

The data and artwork that support the findings of this study
are available from the corresponding author upon reasonable
request.

APPENDIX A: READOUT SYSTEM NOISE
CHARACTERIZATION

The measurement setup for the SDR readout noise characteri-
zation is shown in Fig. 19. It comprises a Direct-RF
Software-Defined Radio (SDR) readout system based on the RFSoC
ZCU216 evaluation kit.[38] In this case, a single tone at frequency
$f_{exc} = 5$ GHz is directly generated in the second Nyquist zone using
high-speed Digital-to-Analog Converter (DAC) sampling at
$f_{DAC} = 8$ GHz. The tone is filtered by a bandpass filter in order to
eliminate spurious components and sent to the receiver (Tx to Rx
loopback). At the receiver side, the tone is amplified by a commer-
cial LNA and filtered again. After that, it is acquired by an
Analog-to-Digital Converter (ADC) in the sixth Nyquist zone.
Finally, it is channelized in the digital domain by a Poly-phase
Filter Bank (PFB), Downconverted to baseband and decimated
using a Digital-Down Converter (DDC). The cutoff frequency of
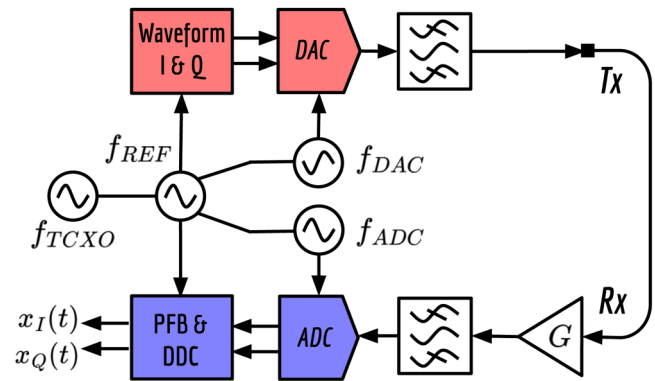
FIG. 19. Noise characterization setup for the Direct-RF Software-Defined Radio
(SDR) readout system based on the RFSoC ZCU216 evaluation kit.[38] A single
tone at $f_{exc} = 5$ GHz is directly generated with the DAC sampling at
$f_{DAC} = 8$ GHz and filtered by a bandpass filter. The tone at the transmitter (Tx)
is sent directly to the receiver port (Rx) where it is amplified and filtered again.
Later, an ADC samples the signal in a higher order Nyquist zone with a sample
rate equal to $f_{ADC} = 2$ GHz. Finally, the tone is channelized by a Poly-Phase
Filter Bank (PFB) and Digitally DownConverted (DDC) to a baseband.

the low-pass filter used in the DDC is $f_{cut} \approx 1.6$ MHz. At this
point, $x_I(t)$ and $x_Q(t)$ components are available at a data rate of
$f_s \approx 15.62$ MHz. This system is equivalent to the homodyne system
presented in Fig. 3. The frequency distribution is performed
through the CLK104 Add-on Board[47] (see Fig. 19). On it, a
Temperature Compensated Crystal Oscillator (TCXO) generates a
10 MHz signal that feed a dual loop jitter cleaner and clock distri-
bution chip (LMK04828B). This chip is responsible for generating
clock signals for the digital system as well as two 250 MHz refer-
ence signals for the DAC and ADC sampling clock synthesizers.
Two different RF synthesizers (LMX2594) connected to the RFSoC
chip generate the $f_{DAC} = 8$ GHz and $f_{ADC} = 2$ GHz sampling
clocks from the 250 MHz references. We are aware that this config-
uration might not be the most suitable one in terms of phase noise
compared to traditional SDR systems using RF mixing
boards.[15,16,23,40] Nevertheless, it is a good example in order to dem-
onstrate the importance of selecting a suitable frequency reference
and clock generation system. Future works include the optimization
of the PLLs and the use of an external ultra-low phase noise refer-
ence (e.g., the rubidium oscillator).

Using the probing tone complex envelope $x_I(t) + jx_Q(t)$,
phase $\phi(t) = \arctan(x_Q(t)/x_I(t))$, and amplitude $\gamma(t)$
$= |x_I(t) + jx_Q(t)|$, time-traces were computed. By means of Python,
$N_s = 2^{24}$ samples were used to calculate readout system phase
$S_\phi^{meas}(f)$ and amplitude $S_\gamma^{meas}(f)$ noise spectra. In order to avoid
spectral leakage, a Blackman–Harris window was applied achieving
a spectral resolution of around ≈ 1 Hz. The resulting spectra for an
ADC input power of $P_{ADC} \approx -5$ dBm ($P_{Tx} \approx -25$ dBm) are shown
in Fig. 4. Equivalently to Eq. (5) with $S_{21} \approx 1$ (i.e., in loopback),
additive and multiplicative noise are measured simultaneously and
cannot be distinguished. This is because the additive noise (orange
noise cloud in Fig. 2) can also be interpreted as simultaneous varia-
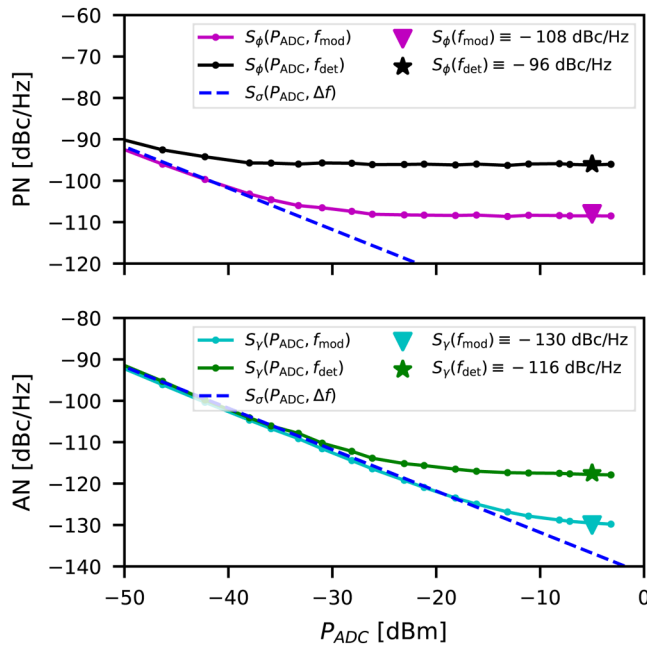tions in phase and amplitude. In this case, the phase $S_\phi^{meas}(f)$ and

amplitude $S_\gamma^{\text{meas}}(f)$ measured spectra consist of the two contributions and can be expressed as

$$S_\phi^{\text{meas}}(f) = S_\phi(f) + \frac{k_B T_n^{ADC}}{P_{ADC}}, \qquad (A1)$$

$$S_\gamma^{\text{meas}}(f) = S_\gamma(f) + \frac{k_B T_n^{ADC}}{P_{ADC}}. \qquad (A2)$$

Here, P_{ADC} is the ADC input power and T_n^{ADC} is the ADC input referred additive noise temperature. The terms on the left side of Eqs. (A1) and (A2) are the pure multiplicative spectra, while the additives are on the right side. In order to extract the pure multiplicative phase and amplitude noise level, a power sweep was performed until the dependence on power vanishes [i.e., $S_\phi^{\text{meas}}(f) \approx S_\phi(f)$ and $S_\gamma^{\text{meas}}(f) \approx S_\gamma(f)$]. The power sweep was performed modifying the DAC output power P_{DAC}. The results of these measurements are shown in Fig. 20. At the top panel, solid black and magenta lines represent the phase noise measured at detector frequencies $S_\phi(P_{ADC}, f_{\text{det}})$ and modulation frequencies $S_\phi(P_{ADC}, f_{\text{mod}})$, respectively. The bottom panel is equivalent, but for the amplitude noise case showing $S_\gamma(P_{ADC}, f_{\text{det}})$ and $S_\gamma(P_{ADC}, f_{\text{mod}})$.

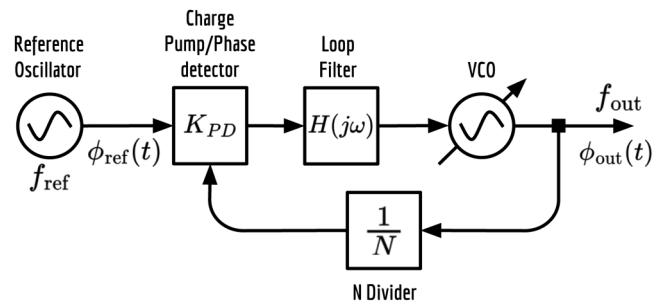At lower powers, both phase and amplitude spectra are dominated by the additive noise following the trajectory indicated with the straight dashed blue line. On the contrary, at high powers, phase and amplitude noise densities are dominated by the multiplicative noise and reach a constant value. As a result, the true phase S_ϕ and amplitude S_γ multiplicative noise values adopted for the analysis described in the main text are $S_\phi(f_{\text{det}}) = -96\,\text{dBc/Hz}$, $S_\phi(f_{\text{mod}}) = -108\,\text{dBc/Hz}$, $S_\gamma(f_{\text{det}}) = -116\,\text{dBc/Hz}$, and $S_\gamma(f_{\text{mod}}) = -130\,\text{dBc/Hz}$. These values are represented by black and green stars, and magenta and cyan triangles in Fig. 20 and in the body of the paper in Fig. 4. Additionally, this procedure allows us to determine the additive noise level from the linear tendency given by the blue dashed line. Using Eq. (10) and considering $S_\sigma(\Delta f) \approx -135\,\text{dBc/Hz}$ at an ADC power of $P_{ADC} \approx -5\,\text{dBm}$, we calculated the ADC input referred additive noise temperature yielding $T_n^{ADC} \approx 724 \cdot 10^3\,\text{K}$. This temperature cannot be directly compared to the cryogenic LNA equivalent noise temperature; therefore, it should be referred to the µMUX output by dividing the noise temperature T_n^{ADC} by the gain G_{Rx} measured between the µMUX output and the ADC input (i.e., $T_n = T_n^{ADC}/G_{Rx}$). Since G_{Rx} is an unknown value and considering that the SDR system was designed properly, we will consider that the SDR system only contributes to multiplicative noise and that the additive noise temperature T_n is dominated by the cryogenic amplifier (e.g., the HEMT or the TWPA[19,20]).

APPENDIX B: SYNTHESIZER PHASE NOISE

The CLK104 Add-on Board is equipped with two wideband Phase-Locked Loop (PLL) synthesizers (LMX2594) used to generate DAC and ADC sampling clocks (see Fig. 19). Most of the phase noise characteristics of the sampling clocks are determined by the PLL components. A simplified block diagram of a PLL is shown in Fig. 21. It comprises five blocks: (1) a reference oscillator, (2) a Voltage-Controlled Oscillator (VCO), (3) a frequency N divider, (4) a loop-filter, and (5) a phase detector.

FIG. 20. Noise spectral densities of a tone at $f_{\text{exc}} = 5\,\text{GHz}$ as a function of ADC input power P_{ADC} measured at frequencies f_{det} and f_{mod}. (top) Phase spectral density $S_\phi(P_{P_{ADC}})$. (bottom) Amplitude spectral density measured at frequencies f_{det} and f_{mod}. (top) Phase spectral density $S_\phi(P_{P_{ADC}})$. The dashed blue straight line represents the additive noise contribution, while dashed black and green stars and magenta and cyan triangles correspond to the phase S_ϕ and amplitude S_γ multiplicative noise values adopted for the analysis and represented in Fig. 4. These values were measured at an ADC input power of $P_{ADC} \approx -5\,\text{dBm}$.

FIG. 21. Phase-Locked Loop (PLL) block diagram. The synthesizer creates a frequency f_{out} from a reference oscillator of N times lower frequency f_{ref}. The feedback system allows the output phase ϕ_{out} to be locked to the reference phase $\phi_{\text{ref}}(t)$. The phase noise response is determined by the noise contributed by each block and the closed-loop gain between each point in the system and the output $\phi_{\text{out}}(t)$.

30 September 2024 12:09:50

When the system is locked, the VCO generates an output frequency f_{out}, which is divided N times and sent to the phase detector. The phase detector compares the phases of the signal coming from the divider $\phi_{out}(t)/N$ with that of the reference oscillator $\phi_{ref}(t)$. At its output, the phase detector (usually implemented as a charge pump) generates a voltage proportional to the phase difference $V_{PD}(t) = K_{PD}(\phi_{ref}(t) - \phi_{out}(t)/N)$. This signal is filtered and used to close the loop by adjusting the VCO voltage $V_{VCO}(t)$ such that the generated frequency is in phase with that of the reference oscillator. In this condition, we can state that the output signal is an exact multiple of the frequency of the reference oscillator $f_{out} = Nf_{ref}$ and follows its phase variations. Typically, the control loop is designed so that the phase error in the steady state is zero [i.e., $\phi_{ref}(t) - \phi_{out}(t)/N = 0$].

The total phase noise $S_\phi^{tot}(\Delta f)$ at the PLL output is determined by the contribution of each of the PLL components. Using the closed-loop gain between each system component and the output $G_i(f)$, it is possible to calculate the total phase noise by adding all noise components $S_\phi^i(\Delta f)$. Using the simulation software provided by the manufacturer, the phase noise of each component of the LMX2594 synthesizer was estimated for the configuration used in the CLK104.[47,48] For demonstration purposes, a $f_{ref} = 250$ MHz reference oscillator with phase noise characteristics $S_\phi^{ref,in}(\Delta f)$ equivalent to a rubidium oscillator was adopted for the simulations.[49] The simulation results for a frequency of $f_{out} = 8$ GHz are shown in Fig. 22. In this case, the synthesizer parameters were optimized to obtain the minimum phase noise in the green shaded region. Only software configurable parameters were modified, avoiding to modify the CLK104 hardware.

The results show that the total phase noise $S_\phi^{tot}(\Delta f)$ for this configuration is determined by the internal components of the synthesizer. At low frequencies, it is dominated by the PLL (divider and phase Detector) noise $S_\phi^{PLL}(\Delta f)$ (dashed orange line), while at higher frequencies, it is dominated by the VCO phase noise $S_\phi^{VCO}(\Delta f)$ (dashed green line). Furthermore, we can conclude that even with the use of a rubidium oscillator, the phase noise is dominated by the PLL circuitry. This is mainly due to three factors: First, the integrated VCO has a high noise level at the operating frequency. Second, the high output frequency imposes a division factor $N = 32$ amplifying both the divider and reference noise by $20 \log_{10}(N)$ (see the magenta line in the figure). Third, the PLL generates electrical noise at the input of the VCO, which creates a strong $1/f$ component given the integrating characteristics of the VCO.[39] Therefore, the phase noise can only be improved by using a higher quality PLL and VCO as well as reducing the value of N by using a higher frequency reference.
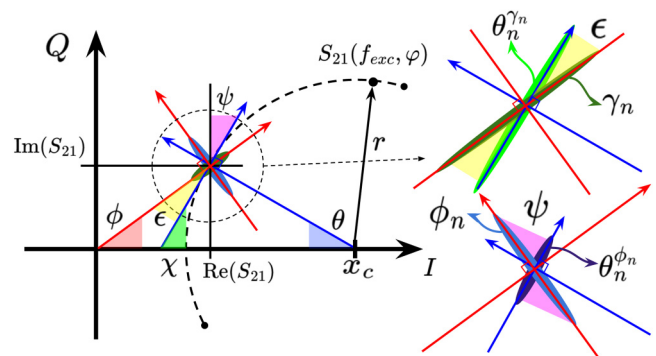
Phase noise present in the ADC or DAC sampling clocks is directly transferred to the generated/acquired tone. In this case, the phase noise is dominated by the DAC sampling at $f_{out} = 8$ GHz. This is consistent with the measurement results shown in Fig. 4 and with the experimental results shown in other articles related to Direct-RF SDR systems based on RFSoC devices used in the field of quantum computing.[25,50] More details about phase noise in PLLs and its optimization can be found in Refs. 39 and 51.

APPENDIX C: NOISE PROJECTIONS

Considering that noise amplitudes are considerably small with respect to $S_{21}(t)$ variations, each noise source can be geometrically projected into the corresponding domain. Figure 23 shows a detailed description of Fig. 2. Defining the readout and resonator's phases as

$$\phi(f_{exc}, \varphi) = \arctan\left\{\frac{\text{Im}[S_{21}(f_{exc}, \varphi)]}{\text{Re}[S_{21}(f_{exc}, \varphi)]}\right\}, \quad (C1)$$

$$\theta(f_{exc}, \varphi) = \arctan\left\{\frac{\text{Im}[S_{21}(f_{exc}, \varphi)]}{x_c - \text{Re}[S_{21}(f_{exc}, \varphi)]}\right\}. \quad (C2)$$

FIG. 22. Phase-locked loop phase noise contributions for a frequency $f_{out} = 8$ GHz generated from a reference frequency of $f_{ref} = 250$ MHz. The solid blue line represents the total phase noise $S_\phi^{tot}(\Delta f)$, while dashed lines are the phase noise contributions $S_\phi^i(\Delta f)$ of each block shown in Fig. 21. The dotted brown line corresponds to the reference oscillator phase noise $S_\phi^{ref,in}(\Delta f)$ at the input, while $S_\phi^{ref,out}(\Delta f)$ is the oscillator phase noise referred to the output.

FIG. 23. Detailed description of the projections of each noise source for both demodulation domains. Amplitude of transmission scattering parameter γ and resonator's phase θ measured from the resonator rotating frame.

Using triangle properties, we easily demonstrate that $\psi = \pi/2 - \epsilon = \theta + \phi$. Therefore, using the adequate trigonometric relations, we can write the projections of amplitude $\gamma_n(t)$ and phase $\phi_n(t)$ readout noise into the resonator's phase $\theta(t)$ as follows:

$$\theta_n^{\gamma_n}(t) \approx \gamma_n(t)\cos(\epsilon) = \gamma_n(t)\frac{\gamma}{r}\sin(\theta + \phi), \quad \text{(C3)}$$

$$\theta_n^{\phi_n}(t) \approx \phi_n(t)\cos(\psi) = \phi_n(t)\frac{\gamma}{r}\cos(\theta + \phi). \quad \text{(C4)}$$

Where the approximation $\theta \approx \Delta_\perp/r$ was used to convert absolute voltage variations into phase units. r stands for the resonance circle radius, while $\Delta_\perp$ represents voltage variations perpendicular to r or, equivalently, tangent to the resonance circle. The noise spectral densities in Table II were calculated considering that, for a given scaling factor g applied to signal $y(t)$, the resulting power spectral density of the scaled signal $z(t)$ is equal to $S_z(\Delta f) = g^2 S_y(\Delta f)$.

REFERENCES

[1]S. Walker, C. E. Sierra, J. E. Austermann, J. A. Beall, D. T. Becker, B. J. Dober, S. M. Duff, G. C. Hilton, J. Hubmayr, J. L. Van Lanen, J. J. McMahon, S. M. Simon, J. N. Ullom, and M. R. Vissers, "Demonstration of 220/280 GHz multichroic feedhorn-coupled TES polarimeter," J. Low Temp. Phys. **199**, 891–897 (2020).
[2]L. Fleischmann, M. Linck, A. Burck, C. Domesle, S. Kempf, M. Rodrigues, A. Pabinger, C. Pies, J.-P. Porst, H. Rotzinger, S. Schäfer, R. Weldle, A. Fleischmann, C. Enss, and G. M. Seidel, "Physics and applications of metallic magnetic calorimeters for particle detection," J. Phys.: Conf. Ser. **150**, 012013 (2009).
[3]J. Zmuidzinas, "Superconducting microresonators: Physics and applications," Annu. Rev. Condens. Matter Phys. **3**, 169–214 (2012).
[4]M. Piat, B. Bélier, L. Bergé, N. Bleurvacq, C. Chapron, S. Dheilly, L. Dumoulin, M. González, L. Grandsire, J.-Ch. Hamilton, S. Henrot-Versillé, D. T. Hoang, S. Marnieros, W. Marty, L. Montier, E. Olivieri, C. Oriol, C. Perbost, D. Prêle, D. Rambaud, M. Salatino, G. Stankowiak, J.-P. Thermeau, S. Torchinsky, F. Voisin, P. Ade, J. G. Alberro, A. Almela, G. Amico, L. H. Arnaldi, D. Auguste, J. Aumont, S. Azzoni, S. Banfi, P. Battaglia, E. S. Battistelli, A. Baü, D. Bennett, J.-Ph. Bernard, M. Bersanelli, M.-A. Bigot-Sazy, J. Bonaparte, J. Bonis, A. Bottani, E. Bunn, D. Burke, D. Buzi, A. Buzzelli, F. Cavaliere, P. Chanial, R. Charlassier, F. Columbro, G. Coppi, A. Coppolecchia, G. D'Alessandro, P. de Bernardis, G. De Gasperis, M. De Leo, M. De Petris, A. Di Donato, A. Etchegoyen, A. Fasciszewski, L. P. Ferreyro, D. Fracchia, C. Franceschet, M. M. Gamboa Lerena, K. Ganga, B. García, M. E. Garc?ía Redondo, M. Gaspard, A. Gault, D. Gayer, M. Gervasi, M. Giard, V. Gilles, Y. Giraud-Heraud, M. Gómez Berisso, M. Gradziel, D. Harari, V. Haynes, F. Incardona, E. Jules, J. Kaplan, A. Korotkov, C. Kristukat, L. Lamagna, S. Loucatos, T. Louis, R. Luterstein, B. Maffei, S. Masi, A. Mattei, A. May, M. McCulloch, M. C. Medina, L. Mele, S. Melhuish, A. Mennella, L. Mousset, L. M. Mundo, J. A. Murphy, J. D. Murphy, F. Nati, C. O'Sullivan, A. Paiella, F. Pajot, A. Passerini, H. Pastoriza, A. Pelosi, M. Percibali, F. Pezzotta, F. Piacentini, L. Piccirillo, G. Pisano, M. Platino, G. Polenta, R. Puddu, P. Ringegni, G. E. Romero, J. M. Salum, A. Schillaci, C. Scoccola, S. Scully, S. Spinelli, M. Stolpovskiy, F. Suarez, A. Tartari, P. Timbie, M. Tomasi, C. Tucker, G. Tucker, S. Vanneste, D. Vigano, N. Vittorio, B. Watson, F. Wicek, M. Zannoni, and A. Zullo, "Qubic: Using NBSI tess with a bolometric interferometer to characterize the polarization of the CMB," J. Low Temp. Phys. **200**, 363–373 (2020).

[5]J. N. Ullom and D. A. Bennett, "Review of superconducting transition-edge sensors for x-ray and gamma-ray spectroscopy," Supercond. Sci. Technol. **28**, 084003 (2015).
[6]L. Gastaldo, K. Blaum, K. Chrysalidis, T. Day Goodacre, A. Domula, M. Door, H. Dorrer, Ch. E. Düllmann, K. Eberhardt, S. Eliseev, C. Enss, A. Faessler, P. Filianin, A. Fleischmann, D. Fonnesu, L. Gamer, R. Haas, C. Hassel, H. Hengstler, J. Jochum, K. Johnston, U. Kebschull, S. Kempf, T. Kieck, U. Köster, S. Lahiri, M. Maiti, F. Mantegazzini, B. Marsh, P. Neroutsos, Yu. N. Novikov, P. C. O. Ranitzsch, S. Rothe, A. Rischka, A. Saenz, O. Sander, F. Schneider, S. Scholl, R. X. Schüssler, Ch. Schweiger, F. Simkovic, T. Stora, Z. Szücs, A. Türler, M. Veinhard, M. Weber, M. Wegner, K. Wendt, and K. Zuber, "The electron capture in 163 Ho experiment—ECHo," Eur. Phys. J. Spec. Top. **226**, 1623–1694 (2017).
[7]S. M. Duff, J. Austermann, J. A. Beall, D. Becker, R. Datta, P. A. Gallardo, S. W. Henderson, G. C. Hilton, S. P. Ho, J. Hubmayr, B. J. Koopman, D. Li, J. McMahon, F. Nati, M. D. Niemack, C. G. Pappas, M. Salatino, B. L. Schmitt, S. M. Simon, S. T. Staggs, J. R. Stevens, J. Van Lanen, E. M. Vavagiakis, J. T. Ward, and E. J. Wollack, "Advanced ACTPol multichroic polarimeter array fabrication process for 150 mm wafers," J. Low Temp. Phys. **184**, 634–641 (2016).
[8]M. H. Abitbol *et al.*, *CMB-S4 Technology Book*, 1st ed. (2017).
[9]K. D. Irwin and K. W. Lehnert, "Microwave squid multiplexer," Appl. Phys. Lett. **85**, 2107–2109 (2004). .
[10]J. Mates, "The microwave SQUID multiplexer," Ph.D. thesis (University of Colorado, 2011).
[11]B. Dober, Z. Ahmed, K. Arnold, D. T. Becker, D. A. Bennett, J. A. Connors, A. Cukierman, J. M. D'Ewart, S. M. Duff, J. E. Dusatko, J. C. Frisch, J. D. Gard, S. W. Henderson, R. Herbst, G. C. Hilton, J. Hubmayr, Y. Li, J. A. B. Mates, H. McCarrick, C. D. Reintsema, M. Silva-Feaver, L. Ruckman, J. N. Ullom, L. R. Vale, D. D. Van Winkle, J. Vasquez, Y. Wang, E. Young, C. Yu, and K. Zheng, "A microwave SQUID multiplexer optimized for bolometric applications," Appl. Phys. Lett. **118**, 062601 (2021).
[12]S. Kempf, M. Wegner, A. Fleischmann, L. Gastaldo, F. Herrmann, M. Papst, D. Richter, and C. Enss, "Demonstration of a scalable frequency-domain readout of metallic magnetic calorimeters by means of a microwave squid multiplexer," AIP Adv. **7**, 015007 (2017).
[13]W. Yoon, J. S. Adams, S. R. Bandler, D. Becker, D. A. Bennett, J. A. Chervenak, A. M. Datesman, M. E. Eckart, F. M. Finkbeiner, J. W. Fowler, J. D. Gard, G. C. Hilton, R. L. Kelley, C. A. Kilbourne, J. A. B. Mates, A. R. Miniussi, S. H. Moseley, O. Noroozian, F. S. Porter, C. D. Reintsema, J. E. Sadleir, K. Sakai, J. S. Smith, T. R. Stevenson, D. S. Swetz, J. N. Ullom, L. R. Vale, N. A. Wakeham, E. J. Wassell, and E. J. Wollack, "Toward large field-of-view high-resolution x-ray imaging spectrometers: Microwave multiplexed readout of 28 TES microcalorimeters," J. Low Temp. Phys. **193**, 258–266 (2018).
[14]R. Gartmann, N. Karcher, R. Gebauer, O. Krömer, and O. Sander, "Progress of the echo SDR readout hardware for multiplexed MMCs," J. Low Temp. Phys. **209**, 726–733 (2022).
[15]C. Yu, Z. Ahmed, J. C. Frisch, S. W. Henderson, M. Silva-Feaver, K. Arnold, D. Brown, J. Connors, A. J. Cukierman, J. M. D'Ewart, B. J. Dober, J. E. Dusatko, G. Haller, R. Herbst, G. C. Hilton, J. Hubmayr, K. D. Irwin, Chao-Lin Kuo, J. A. B. Mates, L. Ruckman, J. Ullom, L. Vale, D. D. Van Winkle, J. Vasquez, and E. Young, "SLAC microresonator RF (SMuRF) electronics: A tone-tracking readout system for superconducting microwave resonator arrays," Rev. Sci. Instrum. **94**, 014712 (2023).
[16]M. E. García Redondo, T. Muscheid, R. Gartmann, J. M. Salum, L. P. Ferreyro, N. A. Müller, J. D. Bonilla-Neira, J. M. Geria, J. J. Bonaparte, A. Almela, L. E. Ardila-Perez, M. R. Hampel, A. E. Fuster, M. Platino, O. Sander, M. Weber, and A. Etchegoyen, "RFSoC Gen3-based software-defined radio characterization for the readout system of low-temperature bolometers," J. Low Temp. Phys. **215**, 161–169 (2024).
[17]K. Sakai, J. S. Adams, S. R. Bandler, D. A. Bennett, K. D. Irwin, and J. A. B. Mates, "Development of space-flight compatible room-temperature

electronics for the Lynx x-ray microcalorimeter," J. Astron. Telesc. Instrum. Syst. **5**, 021013 (2019).

[18]J. M. Geria, M. R. Hampel, S. Kempf, J. J. Bonaparte, L. P. Ferreyro, M. E. G. Redondo, D. A. Almela, J. M. Salum, N. Müller, J. D. Bonilla-Neira, A. E. Fuster, M. Platino, and A. Etchegoyen, "Suitability of magnetic microbolometers based on paramagnetic temperature sensors for CMB polarization measurements," J. Astron. Telesc. Instrum. Syst. **9**(1), 016002 (2023).

[19]N. Zobrist, B. H. Eom, P. Day, B. A. Mazin, S. R. Meeker, B. Bumble, H. G. LeDuc, G. Coiffard, P. Szypryt, N. Fruitwala, I. Lipartito, and C. Bockstiegel, "Wide-band parametric amplifier readout and resolution of optical microwave kinetic inductance detectors," Appl. Phys. Lett. **115**, 042601 (2019).

[20]M. Malnou, J. A. B. Mates, M. R. Vissers, L. R. Vale, D. R. Schmidt, D. A. Bennett, J. Gao, and J. N. Ullom, "Improved microwave SQUID multiplexer readout using a kinetic-inductance traveling-wave parametric amplifier," Appl. Phys. Lett. **122**, 214001 (2023).

[21]C. Yu, Z. Ahmed, J. M. D'Ewart, J. C. Frisch, S. W. Henderson, and M. Silva-Feaver, "A simulation suite for readout with SMuRF tone-tracking electronics," Proc. SPIE **12190**, 121900V (2022).

[22]C. Schuster, M. Wegner, and S. Kempf, "Simulation framework for microwave SQUID multiplexer optimization," J. Appl. Phys. **133**, 044503 (2023).

[23]J. van Rantwijk, M. Grim, D. van Loon, S. Yates, A. Baryshev, and J. Baselmans, "Multiplexed readout for 1000-pixel arrays of microwave kinetic inductance detectors," IEEE Trans. Microw. Theory Tech. **64**, 1876–1883 (2016).

[24]J. Herrmann *et al.*, "Frequency up-conversion schemes for controlling superconducting qubits," arXiv:2210.02513 (2022).

[25]C. Ding, M. Di Federico, M. Hatridge, A. Houck, S. Leger, J. Martinez, C. Miao, D. S. I, L. Stefanazzi, C. Stoughton, S. Sussman, K. Treptow, S. Uemura, N. Wilcer, H. Zhang, C. Zhou, and G. Cancelo, "Experimental advances with the QICK (quantum instrumentation control kit) for superconducting quantum hardware," Phys. Rev. Res. **6**, 013305 (2024).

[26]M. Wegner, C. Enss, and S. Kempf, "Analytical model of the readout power and SQUID hysteresis parameter dependence of the resonator characteristics of microwave squid multiplexers," Supercond. Sci. Technol. **35**, 075011 (2022).

[27]F. K. Ahrens, "Cryogenic read-out system and resonator optimisation for the microwave SQUID multiplexer within the ECHo experiment," Ph.D. thesis (Heidelberg University, 2022).

[28]S. Probst, F. Song, P. Bushev, A. Ustinov, and M. Weides, "Efficient and robust analysis of complex scattering data under noise in microwave resonators," Rev. Sci. Instrum. **86**, 024706 (2014).

[29]J. A. B. Mates, K. D. Irwin, L. R. Vale, G. C. Hilton, J. Gao, and K. W. Lehnert, "Flux-ramp modulation for SQUID multiplexing," J. Low Temp. Phys. **167**, 707–712 (2012).

[30]M. Silva-Feaver, M. Silva-Feaver, Z. Ahmed, K. Arnold, J. C. Frisch, J. Groh, S. W. Henderson, J. Vasquez, and C. Yu, "Phase drift monitoring for tone tracking readout of superconducting microwave resonators," Proc. SPIE **12190**, 417 (2022).

[31]M. Sathyanarayana Rao, M. Silva-Feaver, A. Ali, K. Arnold, P. Ashton, B. J. Dober, C. J. Duell, S. M. Duff, N. Galitzki, E. Healy, S. Henderson, S.-P. Ho, J. Hoh, A. M. Kofman, A. Kusaka, A. T. Lee, A. Mangu, J. Mathewson, P. Mauskopf, H. McCarrick, J. Moore, M. D. Niemack, C. Raum, M. Salatino, T. Sasse, J. Seibert, S. M. Simon, S. Staggs, J. R. Stevens, G. Teply, R. Thornton, J. Ullom, E. M. Vavagiakis, B. Westbrook, Z. Xu, and N. Zhu, "Simons observatory microwave SQUID multiplexing readout-cryogenic RF amplifier and coaxial chain design," J. Low Temp. Phys. **199**, 807–816 (2020).

[32]J. M. Salum, M. E. García Redondo, L. P. Ferreyro, J. Bonilla-Neira, N. Müller, J. M. Geria, J. Bonaparte, T. Muscheid, R. Gartmann, A. Fuster, A. Almela,

M. R. Hampel, L. E. Ardila-Perez, O. Sander, S. Kempf, M. Platino, M. Weber, and A. Etchegoyen, "Spectral engineering for optimal signal performance in the microwave squid multiplexer," J. Low Temp. Phys. **214**, 272 (2024).

[33]E. Rubiola, *Phase Noise and Frequency Stability in Oscillators*, The Cambridge RF and Microwave Engineering Series (Cambridge University Press, 2008).

[34]Rohde & Schwarz GmbH & Co. KG, "Understanding phase noise measurement techniques," white paper, 2021.

[35]Rohde & Schwarz GmbH & Co. KG, "Understanding phase noise fundamentals," version 01.01, Rohde & Schwarz GmbH & Co. KG, 2021.

[36]J. Gao, J. Zmuidzinas, B. A. Mazin, H. G. LeDuc, and P. K. Day, "Noise properties of superconducting coplanar waveguide microwave resonators," Appl. Phys. Lett. **90**, 102507 (2007).

[37]S. Kumar *et al.*, "Temperature dependence of the frequency and noise of superconducting coplanar waveguide resonators," Appl. Phys. Lett. **92**, 123503 (2008).

[38]AMD, "ZCU216 evaluation board user guide (UG1390)," (2022).

[39]A. Hajimiri, "Noise in phase-locked loops," in *2001 Southwest Symposium on Mixed-Signal Design (Cat. No.01EX475)*, Austin, TX, USA (IEEE, 2001), pp. 1–6.

[40]J. D. Gard, D. T. Becker, D. A. Bennett, J. W. Fowler, G. C. Hilton, J. A. B. Mates, C. D. Reintsema, D. R. Schmidt, D. S. Swetz, and J. N. Ullom, "A scalable readout for microwave squid multiplexing of transition-edge sensors," J. Low Temp. Phys. **193**, 485–497 (2018).

[41]D. Becker, D. Bennett, M. Biasotti, M. Borghesi *et al.*, "Working principle and demonstrator of microwave-multiplexing for the Holmes experiment microcalorimeters," J. Instrum. **14**, P10035 (2019).

[42]N. Karcher, T. Muscheid, T. Wolber, D. Richter, C. Enss, S. Kempf, and O. Sander, "Online demodulation and trigger for flux-ramp modulated SQUID signals," J. Low Temp. Phys. **209**, 581–588 (2022).

[43]J. M. Salum, T. Muscheid, A. Fuster, M. E. Garcia Redondo, M. R. Hampel, L. P. Ferreyro, J. M. Geria, J. Bonilla-Neira, N. Müller, J. Bonaparte, A. Almela, L. E. Ardila-Perez, M. Platino, O. Sander, and M. Weber, "Aliasing effect on flux ramp demodulation: Nonlinearity in the microwave squid multiplexer," J. Low Temp. Phys. **213**, 223–236 (2023).

[44]L. Ferreyro, M. G. Redondo, M. Hampel, A. Almela, A. Fuster, J. Salum, J. Geria, J. Bonaparte, J. Bonilla-Neira, N. Müller, N. Karcher, O. Sander, M. Platino, M. Weber, and A. Etchegoyen, "An implementation of a channelizer based on a Goertzel filter bank for the read-out of cryogenic sensors," J. Instrum. **18**, P06009 (2023).

[45]P. Welch, "The use of fast Fourier transform for the estimation of power spectra: A method based on time averaging over short, modified periodograms," IEEE Trans. Audio Electroacoust. **15**, 70–73 (1967).

[46]C. M. Caves, "Quantum limits on noise in linear amplifiers," Phys. Rev. D **26**, 1817–1839 (1982).

[47]AMD, "CLK104 RF clock add-on card user guide (UG1437)," (2022).

[48]Version 1.6.7, PLLatinum simulator tool, Texas Instruments, 2024, https://www.ti.com/tool/PLLATINUMSIM-SW

[49]S. R. Systems, FS725—Benchtop rubidium frequency standard, https://www.thinksrs.com/downloads/pdfs/catalog/FS725c.pdf

[50]L. Stefanazzi, K. Treptow, N. Wilcer, C. Stoughton, C. Bradford, S. Uemura, S. Zorzetti, S. Montella, G. Cancelo, S. Sussman, A. Houck, S. Saxena, H. Arnaldi, A. Agrawal, H. Zhang, C. Ding, and D. I. Schuster, "The QICK (quantum instrumentation control kit): Readout and control for qubits and detectors," Rev. Sci. Instrum. **93**, 044709 (2022).

[51]A. Hajimiri and T. Lee, "A general theory of phase noise in electrical oscillators," IEEE J. Solid-State Circuits **33**, 179–194 (1998).

30 September 2024 12:09:50